

Accepted 10/23/2019

Journal of Geology

Genesis and Petrology of Post-collisional Rare metal-bearing Granites in the Arabian Shield: A case study of Aja Ring Complex, Northern Saudi Arabia

Bassam A. Abuamarah

*Department of Geology and Geophysics, King Saud University, Riyadh 11451, Saudi
Arabia*

Abstract

The Jabal Aja Ring Complex (ARC) is a Late Ediacaran composite pluton of post-collisional A-type granites in the northeastern part of the Arabian Shield. It is an elliptical body with discontinuous ring-shaped outcrops due to later faulting. Field relationships enable the recognition of two main phases of magmatic activity in the ARC. The early phase represents the core of the intrusion (monzogranite, syenogranite, granophyre, and alkali feldspar granite) surrounded by the last phase (alkali volcanics and alkaline/peralkaline granites). The contacts between two phases are gradational and/or sharp, indicating their emplacement within a very short time period before the complete crystallization of the earlier phase. The ARC is alkaline to peralkaline rare-metal granites with the common geochemical characteristics of post-collisional intraplate A-type rocks. The pronounced negative Eu anomalies ($\text{Eu}/\text{Eu}^* = 0.14\text{--}0.25$) reflect extreme magmatic fractionation and perhaps the effects of late fluid–rock interaction. All A-type rocks of the ARC retain a positive Nb-Ta anomaly that increases from the early phase to the most evolved alkaline/peralkaline granites. They define geochemical signatures reflecting their derivation from same magma sources that evolved through fractional crystallization with crustal contamination. The geochemical characteristics of the A-type granites of ARC reflect re-melting

of previously formed arc material. The mafic microgranular enclaves (MMEs) represent metamorphic rocks derived from/in the deeper part of the crust, and represent the source rocks from which the granitic magma was generated by partial melting. The early phase of magmatism of the ARC represents melts derived from partial melting of lower/middle crustal sources during the post-collisional stage that fractionated to give the various granitic rocks. The absence of mafic xenoliths in the late stage of the ARC indicates that the contribution of crustal sources to the magma generation is absent in the late stage.

Keywords: Arabian Shield, post-collisional, rare-metal bearing granite, ring complex, anorogenic.

1. Introduction

The Jabal Aja igneous complex represents a late Neoproterozoic ring complex that forms a part of the juvenile continental crust of the Arabian–Nubian Shield (ANS) exposed on the Western and Eastern flanks of the Red Sea (Stern 2002; Meert 2003; Johnson 2003; Hargrove et al. 2006; Stoeser and Frost 2006; Ali et al. 2010). The ANS represents a collage of ophiolite sequences and associated volcanic arcs, which amalgamated during the assembly of West and East Gondwana land and then intruded by different granitoids and mafic-ultramafic intrusions (e.g., Stern 1994; Stein and Goldstein 1996; Genna et al. 2002; Meert 2003; Johnson and Woldehaimanot 2003; Stoeser and Frost 2006; Ali et al. 2010; Azer et al. 2017).

The juvenile continental crust of the Arabian shield evolved in Neoproterozoic time (850–590 Ma) through three main phases including pre-collisional, collisional, and post-collisional (Stern 1994, 2002; Patchett and Chase 2002; Stoeser and Frost 2006; Stoeser and Camp 1985; Johnson and Woldehaimanot 2003). The first phase (870–700 Ma) started with the

emplacement of ophiolitic rocks, metamorphosed calc-alkaline metagabbro-diorite-granitoid, and associated volcano-sedimentary successions. This phase was followed by the emplacement of calc-alkaline arc magmatism (670–630 Ma), which produced less deformed calc-alkaline gabbro-diorite complexes and granodiorites with their equivalent volcanics (e.g., Moghazi et al. 1999; Farahat et al. 2011; Basta et al. 2017; Maurice et al. 2018; Samuel et al. 2019). The post-collisional stage (~620–580 Ma) is represented by un-deformed calc-alkaline and alkaline granites, and was terminated by the production of less abundant peralkaline granites and volcanics (e.g., Samuel et al. 2007; Eyal et al. 2014; Ali et al. 2014, 2015; Khalil et al. 2018; Azer et al. 2014; Gahlan et al. 2016). The wide distribution of post-collisional calc-alkaline and alkaline/peralkaline granitoids in the Arabian Shield is of geodynamic interest owing to the significant addition of crustal material into the juvenile crust of the Arabian Shield over a short period of time.

In the Arabian Shield, granitic rocks were emplaced at various crustal levels with variable ages, tectonic settings, and geochemical characteristics (e.g., Stoeser and Elliott 1980; Jackson 1986; Stoeser 1986; Elliott et al. 1999; Moufti et al. 2002, Qadhi 2007; Küster 2009; Ali et al. 2014; Moghazi et al. 2015). The Neoproterozoic Arabian Shield hosts a number of discrete A-type igneous complexes of shallow emplacement, with significant enrichment of rare metals (e.g., Drysdall et al. 1984; Harris 1985; Ramsay et al. 1986; Jackson and Douch 1986; Drysdall and Douch 1986; Hackett 1986; Qadhi 2007; Elliott et al. 1999; Moghazi et al. 2011, 2015; Ali et al. 2014). Despite widespread outcrops and several previous studies in the Arabian Shield, the geotectonic evolution and petrogenesis of A-type granites remain controversial.

The Aja Ring complex (ARC), the subject of this study, provides a good example of post-collisional alkaline and peralkaline granites. With the exception of few published papers (e.g.,

[Ekren et al. 1987](#); [Qadhi 2007](#)), no detailed previous studies have been carried out on the ARC. This work presents detail geological, mineralogical, and geochemical data on the A-type granites of the ARC. Bulk geochemistry (major, trace, and rare-earth elements) coupled with mineral chemistry are used to investigate the petrogenesis of the A-type granitic magmas and deduce their sources. We used the present data to understand the formation of the juvenile continental crust of the ANS during Neoproterozoic time. We then integrate these results with published geochemical and geochronological data to discuss the significance of the A-type magmatism in the geotectonic evolution of the northernmost ANS.

2. Geological setting

The ARC is exposed at the northeastern-most section of the Arabian Shield to the west of Hail town (**Fig. 1**), where it appears as a high mountainous area of crystalline Neoproterozoic igneous rocks. The ARC extends in a NE-SW direction as a composite granitic pluton. The long axis of the pluton extends to approximately 50 km and its maximum width approaches 35 km. The ARC is dissected by many wadis, which are structurally controlled and delineate the predominant fault systems. The area under investigation lies between latitudes the $27^{\circ} 20' N$ & $27^{\circ} 40' N$ and longitudes $41^{\circ} 20' E$ & $41^{\circ} 40' E$. Until now, the ARC has not been studied in great detail; the different rock types of the ARC have been studied separately. A lack of detailed field works has led to a misunderstanding of the relationships between the different rock units of the ARC and their distribution. [Stuckless et al. \(1984\)](#) obtained 570 ± 19 Ma for the granitic rocks of the ARC. [Ekren et al. \(1987\)](#) prepared a detailed geological map of the Hail area at a scale of 1:250,000, showing the distribution of various granitic rocks of the Aja igneous complex. The granitic rocks of the Aja complex were distinguished by [Qadhi \(2007\)](#) into five

varieties: albite granites, alkali feldspar granite, granophyre, alkaline granite, and peralkaline granite. [Herrher and Abdallah \(2017\)](#) applied a remote sensing technique to distinguish spectral variations among the mineral suits of igneous rocks of the ARC.

The country rocks of the ARC are covered by wide alluvial deposits, concealing a larger extent of the intrusion. The ARC occurs as large isolated pluton of irregular shape, elongated in a NE-SW direction (**Fig. 2**). It consists of late Neoproterozoic rocks, including different granitoids and volcanic rocks. The granitoids are emplaced as successive intrusions marked by a variation in their colors, textures, and compositions. Based on present field work, two phases of granitoids are distinguished, which are separated by extrusive volcanics. The early phase represents the inner core of the ARC, including monzogranite, syenogranite, granophyre, and alkali feldspar granite, and the second phase represents the outer rims, including alkaline and peralkaline granites.

Monzogranite represents the oldest rock unit in the mapped area and occupies the core of the ARC. It is coarse- to medium-grained and highly weathered, forming low-lying land (**Fig. 3a**). In few outcrops, it shows a porphyritic nature. It is completely engulfed by granophyre and intruded by alkali feldspar granite with sharp intrusive contacts. Many mafic microgranular enclaves (MMEs) and gneiss xenoliths are observed within the monzogranite. Syenogranite intrudes into the monzogranite and in turn is intruded by granophyre, alkali feldspar granite, and alkaline/peralkaline granites. The granophyre is predominant among the granites, forming moderate to high-relief hills. It intrudes into the monzogranite and syenogranite, and is truncated by the alkali feldspar granite in addition to the alkaline/peralkaline granites. Some roof pendants of the granophyre are observed above the alkaline/peralkaline granites. The alkali feldspar granite has a pinkish red to brick red color and occurs in small bodies intruded into the

syenogranite and granophyre and truncated by alkaline/peralkaline granites (**Fig. 3b**). The contacts between the granophyre and alkali feldspar granites are gradational and irregular. The alkali feldspar granite is affected by significant alterations due to the intrusion of the alkaline/peralkaline granites.

The alkali volcanics are observed only in the northern part of the ARC. They appear as roof pendant above granophyre (**Fig. 3c**), and intruded by alkaline/peralkaline granites. The alkali volcanics are fine-grained rocks with a grayish-green color and show porphyritic texture. They constitute a stratified sequence of pyroclastic, ignimbrites, and rhyolite flows. Alkaline/peralkaline granites form irregular-shaped bodies and occur as discontinuous, ring-shaped outcrops forming the outer rims of the ARC. The alkaline granite is more abundant in the western part of the ARC, whereas the peralkaline granite is well exposed in the eastern rim of the ARC. The contacts between the alkaline and peralkaline granites are mostly gradational, but they are sharp in some cases, indicating their emplacement with a very short time interval, still before complete crystallization of the earlier batch. Within 50 to 200 m of alkaline/peralkaline granites, the inner core rocks are characterized by various degrees of alterations that decrease away from the outer rims. The outcrops of alkaline/peralkaline granites reach elevations of 1400–1600 m (a.s.l.) and are characterized by steep, smooth, dipping slopes. Several apophyses of these granites extend into the inner core. A conspicuous feature of the alkaline/peralkaline granites of the ARC is a lack of MMEs and dykes, in contrast to the presence of such features in the early phase (inner core). Some roof pendants of granophyre and alkali volcanics are observed above the alkaline/peralkaline granites, especially in its northern portions. Few pegmatitic veins and miarolitic cavities are observed cutting the eastern outer rim of the ARC.

Some dykes are observed cutting the early phase of the ARC, especially the monzogranite and in turn, intruded by late granitic phases (**Fig. 3a**). These dykes are black-colored and are mainly mafic in their composition, showing a close resemblance to the isolated MMEs of their host granites. The contacts of the dykes with their host granites are almost sharp, and no criteria for hybridization or reaction are observed. These dykes may be synplutonic mafic magma globules that were coevally and synchronously injected into the more felsic, still mobile and crystallizing phase.

Few MMEs and gneiss xenoliths are observed in the monzogranite. They vary from 5 to 25 cm in diameter. The MMEs have an ellipsoid shape with ovoid and rounded outlines in the outcrops. This shape may be due to the deformation of enclaves during the motion and emplacement of granitic magma. The gneiss xenoliths are subrounded to irregular in shapes and represent accidental fragments of old juvenile crustal rocks. They show textural effects of thermal metamorphism. The contacts between the MMEs and xenoliths within the hosting granites are almost sharp, but slightly reaction contacts are observed. In some rare cases, only ghosts of the enclaves are preserved, as indicated by patches of higher concentration of mafics within the lighter-colored granite host. In spite of the prevalent microgranular nature of the MMEs, some of them possess large white plagioclase crystals (up to 7 mm across). Additionally, a few pink alkali feldspar crystals may lie across the contacts between MMEs and the granite host. The MMEs send small trails of amphibole crystals into the host granite. This is attributed to crystal transfers between two coeval magmas during magma mixing processes.

3. Petrography

The granitic rocks of the ARC show wide variations in their textures and mineralogical compositions. Based on the modal classification of [Streckeisen \(1976\)](#), the early phase of the A-type granites of the ARC are monzogranite, syenogranite, granophyre, and alkali feldspar granite, and the later phase includes alkaline granite and peralkaline granite. Brief petrographic descriptions of the different granitic rocks and MMEs are given in the following.

3.1. Monzogranite

Monzogranite is inequigranular, medium- to coarse-grained, and pink to pale pink in color. It consists essentially of K-feldspar (30–45%), quartz (25–35%), plagioclase (15–25%), and some mafic minerals (<5%). Opaques, titanite, zircon, and apatite are accessories. The K-feldspars occur as large anhedral crystals of orthoclase perthite (string perthites) containing small plagioclase prisms as inclusions. The quartz occurs as anhedral to subhedral crystals, occupying the interstitial spaces between the feldspars. Locally, the quartz forms graphics and myrmekitic intergrowths. Plagioclase occurs as euhedral to subhedral tabular crystals, which are usually corroded and enclosed in coarse perthitic orthoclase (**Fig. 4a**). The mafic minerals include biotite and hornblende. The biotite is the dominant mafic mineral and occurs as anhedral flakes or as anhedral interstitial prisms in the spaces between the quartz and feldspars. Hornblende is very rare and occurs as fine-grained prismatic crystals.

3.2. Syenogranite

Syenogranite is medium- to coarse-grained with a hypidiomorphic, inequigranular texture. It consists of K-feldspars (40–55%) and quartz (20–25%), with variable amounts of plagioclase (4–12%) and mafic minerals (1.5–2.5%). Accessory minerals include Fe-Ti oxides, zircon, titanite, and apatite. A few quartz and K-feldspar crystals display micrographic

intergrowths. Perthite is the dominant K-feldspar, including flame, patchy, and veined types. 184
Rare albite and biotite crystals are observed within the perthite. The quartz occurs as anhedral 185
aggregates or as fine crystals within perthite. The mafic minerals include mainly biotite and rare 186
amphibole. The biotite occurs as subhedral tabular crystals (**Fig. 4b**) or forms aggregates with 187
opaque minerals. Amphibole is strongly pleochroic and occurs as small anhedral to subhedral 188
fine crystals. 189

3.3. *Granophyre* 191

Granophyre is a porphyritic rock, composed mainly of K-feldspar and plagioclase 192
phenocrysts, set in a fine- to medium-grained groundmass of quartz, K-feldspars, opaque, and a 193
few mafic minerals. The plagioclase is represented mainly by albite, which occurs as large, stout 194
prisms, usually fresh and twinned. The K-feldspars are intergrown with quartz, forming a 195
micrographic intergrowth texture. The quartz occurs also as small anhedral to subhedral 196
phenocrysts. The K-feldspar phenocrysts occur as rectangular crystals. Graphic intergrowths are 197
common in the groundmass and surrounding the K-feldspars and quartz microphenocrysts. The 198
mafic minerals are rare and include fine biotite flakes in the groundmass. 199

3.4. *Alkali feldspar granite* 201

Alkali feldspar granite is coarse-grained with an allotriomorphic texture, composed 202
essentially of K-feldspars (40–50%), quartz (20–30%), and plagioclase (5–10%). Opaques, 203
biotite, muscovite, titanite, apatite, zircon, and fluorite are accessories. The K-feldspars occur as 204
subhedral to anhedral orthoclase perthite and microcline perthite, occupying the interstitial 205
spaces of other constituents. They show simple twinning with corroded outlines and enclose 206

albite inclusions. Late-crystallized orthoclase is observed as rims around the orthoclase perthites. Microcline perthite occurs in very subordinate amounts, and shows cross-hatching twinning (**Fig. 4c**). The quartz occurs as anhedral to subhedral crystals occupying the interstitial spaces and forming graphic texture with the feldspars. Plagioclase is represented by subhedral and anhedral twinned albite, which is corroded by the quartz and K-feldspars. Fe-Ti oxides occur as disseminated fine crystals or as anhedral fine aggregates after altered mafic minerals. The biotite and muscovite occur as flakes or as tabular crystals, varying in their amounts among samples (**Fig. 4d**). Fluorite occurs as anhedral interstitial crystals or as vein filling along fractures traversing the rock. A few wedge-shaped crystals of titanite and euhedral crystals of allanite are observed in a limited number of samples. Fine apatite needles and separate zircon crystals (**Fig. 4e**) are interstitial among the feldspars.

3.5. Alkaline and peralkaline granites

Alkaline granite is medium- to coarse-grained with a hypersolvous and hypidiomorphic granular texture. It consists of K-feldspars (40–50%), quartz (25–35%), plagioclase (<7%), and mafic minerals (3–7%). The accessory minerals include Fe-Ti oxides, allanite, zircon, titanite, monazite, apatite, sphene, columbite, xenotime, thorite, and fluorite. K-feldspars include orthoclase perthite and microcline. The perthitic crystals show flame, patchy, and vein-perthitic intergrowth types as well as zebra bands of K-feldspar and albite with irregular boundaries. The microcline crystals show cross-hatching with rare small inclusions of albite and biotite crystals. Quartz occurs as anhedral to euhedral interstitial crystals or forming micrographic intergrowths with K-feldspars. A Few quartz crystals contain tiny inclusions of the mafic minerals and feldspars. Plagioclase is represented only by albite, which occurs as subhedral laths or as

inclusions in the perthite and quartz crystals. The mafic minerals are represented mainly by sodic amphibole (**Fig. 4f, g**). They occur as subhedral to anhedral crystals or acicular crystals interstitial between the essential minerals. Locally, they are altered along their margins into aggregates of Fe-Ti oxides. Rare zircon inclusions are observed within the sodic amphiboles.

Fluorite is the most common accessory mineral, occurring as discrete crystals in interstices between other minerals (**Fig. 4h**) or as veinlets suggesting a deuteric origin (Tollo et al. 2004). Strongly pleochroic reddish-brown anhedral crystals of allanite are observed in certain thin sections associated with sodic amphibole (**Fig. 4i**). Both secondary and primary muscovites are distinguished in alkaline granite. The primary muscovite occurs as subhedral to euhedral crystals or forms clots of several crystals (**Fig. 4j**), whereas the secondary muscovite occurs mainly as fine anhedral crystals replacing feldspars. Zircon occurs as clear euhedral separated crystals or as inclusions in the mafic minerals. A few euhedral to subhedral crystals of monazite and titanite are observed in association with iron oxides. A few anhedral brownish black crystals of columbite and thorite are recorded in a number samples (**Fig. 4 k**). Fe-Ti oxides occur either as individual crystals or as granular aggregates associated with altered mafic minerals, and apatite occurs as fine needles.

Peralkaline granite is similar in its composition to alkaline granite, with minor differences. It contains more modal K-feldspars (50–60%) and alkaline mafic minerals (5-15%) than the alkaline granite. The peralkaline granite has wide variations of accessory minerals, similar to the alkaline granite. The mafic minerals include sodic amphibole and sodic pyroxene with minor muscovite. The sodic amphibole occurs as euhedral to subhedral prismatic sparse crystals between the essential minerals, including riebeckite and arfvedsonite. They contain small inclusions of zircon and Fe-Ti oxides. A few sodic amphibole crystals show slight

alterations along their margins into opaques and chlorite. Sodic pyroxenes occur as euhedral to subhedral prismatic crystals, including aegirine and aegirine-augite associated with allanite (**Fig. 4l**).

3.6. Mafic microgranular enclaves (MMEs)

MMEs of various shapes and sizes are observed in monzogranite. They are fine- to medium-grained with an equigranular texture. They are mainly diorite in composition and have chilled margins, indicating rapid cooling. They consist essentially of plagioclase, amphibole, and biotite with variable amounts of opaques, K-feldspars, and apatite. Occasional large plagioclase and K-feldspars xenocrysts with irregular outlines, and spongy cellular texture are observed, indicating resorption under disequilibrium conditions.

4. Analytical methods

Based on the petrographic studies, a set of fresh samples were selected for whole-rock and microprobe analyses. Twenty-one samples representing the post-collisional A-type granitic rocks of the ARC and three samples of the MMEs were selected for bulk chemical analysis. Whole rock chemical analyses for major, trace, and rare-earth elements were carried out at the Activation Laboratories Ltd. in Ontario, Canada. Major oxide compositions and Ba, Co, Cu, Nb, Ni, Sc, Sr, Y, Zn, and Zr elements were analyzed using inductively coupled plasma atomic emission spectrometry (ICP-AES). The rare-earth elements and some of the trace elements were determined using inductively coupled plasma mass spectrometry (ICP-MS) following a lithium metaborate/tetraborate fusion and nitric acid digestion of a 0.2 g sample. The loss on ignition

(LOI) was measured using the OA-GRA05 method by measuring the difference in mass after heating to 1000 °C using a WST-SEQ instrument.

Mineral chemistry data of different representative minerals were acquired using a JEOL JXA-8500F electron microprobe at Washington State University (WSU). The analytical conditions consisted of a 15 kV accelerating voltage, 20 nA probe current, and 1 µm beam diameter, with a counting time of 10 s on peak. Combinations of suitable natural and synthetic mineral standards were applied for calibration. The standards used for calibration were MgO for Mg, orthoclase for K, albite for Na, wollastonite for Ca and Si, pyrophanite for Mn and Ti, aluminum oxide for Al, and fayalite for Fe. The analytical precision and detection limits of the analyses performed at WSU are listed on the website of the laboratory (<https://environment.wsu.edu/facilities/geoanalytical-lab>). Complete microprobe analyses of different minerals are given in the online version (Supplementary Tables 1S–9S).

5. Mineral chemistry

The identification of the minerals under the microscope was refined and supported by electron microprobe analyses. The essential silicate minerals were analyzed in samples of monzogranite, syenogranite, alkali feldspar granite, alkaline granite, and peralkaline granite. The analyzed minerals included feldspars, pyroxene, biotite, muscovite, and amphibole. The chemical formulae of the analyzed minerals were processed and calculated using the software package Minpet (Richard 1995). All the electron microprobe analyses of different minerals are given in Supplementary Tables 1S–9S.

The chemical composition, calculated structural formulae based on 32 oxygen atoms, and end-member components of the analyzed feldspars are given in Supplementary Tables 1S–5S.

The analyzed feldspars are represented by plagioclase, albite, and K-feldspars. The plagioclases were analyzed from monzogranite, syenogranite, and alkali feldspar granite. The CaO contents in the analyzed plagioclase decrease from monzogranite (4.16–5.78 wt.%) to syenogranite (3.48–4.32 wt.%) (Supplementary Table 2S), and alkali feldspar granite (3.12–3.45 wt.%). The plagioclases are mainly oligoclase ((An_{13.04–23.84}). Albite is analyzed from all the rock types. It has a high Na₂O content, which increases from monzogranite (10.63–11.00 wt.%) to peralkaline granite (11.50–11.75 wt.%), whereas the CaO content is low and decreases from monzogranite (0.25–0.96 wt.%) to peralkaline granite (0.03–0.26 wt.%). K-feldspars have a high K₂O content, which increases from monzogranite (14.45–15.60 wt.%) to peralkaline granite (16.23–16.50 wt.%). The Or contents range from 90 to 95 in monzogranite, 95 to 98 in syenogranite, ~98 in alkali feldspar granite, ~98 alkaline granite, and 98–99 in peralkaline granite. CaO is low in all the analyzed K-feldspar crystals, with a maximum concentration of 0.18 wt.%.

Some pyroxene crystals were analyzed in the alkaline and peralkaline granites of the ARC and their chemical compositions are listed in Supplementary Table 6S. They are sodic pyroxene with high contents of Na₂O (11.46–12.97 wt.%) and FeO (24.18–26.49 wt.%) with variable amounts of Al₂O₃ (2.99–4.75 wt.%), TiO₂ (2.33–4.76 wt.%), CaO (0.03–1.34 wt. %), MgO (0.02–2.60 wt.%), and K₂O (<0.93 wt. %). According to the classification scheme of Morimoto et al. (1988), the analyzed pyroxene crystals are classified as aegirine (**Fig. 5a**).

Biotite was analyzed in monzogranite, syenogranite, and alkali feldspar granite. The chemical analyses of the biotite crystals and their structural formulae calculated on the basis of 22 oxygen atoms in the anhydrous total are given in Supplementary Table 7S. The analyzed biotites show wide variation in SiO₂ (34.84–37.66 wt.%), TiO₂ (3.69–4.85 wt.%), Al₂O₃ (11.29–12.47wt.%), FeO (21.15–30.09 wt.%), MgO (3.99–10.16 wt.%), and K₂O (7.89–9.27 wt.%). On

the ternary discrimination diagram of Nachit [et al. \(2005\)](#), they all appear in the igneous biotite field (**Fig. 5b**). Nachit [et al. \(1985\)](#) and Abdel-Rahman (1994) assumed that the composition of biotite indicates the nature of the original parent magma. They used biotite chemistry to discriminate among peraluminous, calc-alkaline, and alkaline-peralkaline granites. On the Al vs. Mg discrimination diagram of Nachit [et al. \(1985\)](#), they analyzed the biotite crystals of the ARC in the alkaline/peralkaline field (**Fig. 5c**). Additionally, on the biotite discrimination diagram of Abdel-Rahman (1994), they appear in the field of alkaline rocks (**Fig. 5d**).

Muscovite was analyzed in alkali feldspar granite, alkaline granite, and peralkaline. Chemical analyses of the muscovite and its structural formulae are given in Supplementary Table 8S. On the petrographical criteria such as medium grain size and subhedral to euhedral shape, the analyzed muscovite is judged to be primary. The analyzed muscovite crystals have $\text{TiO}_2 > 0.6$ wt.%, comparable to muscovite of magmatic origin (e.g., Zen 1988; Villa [et al. 1997](#)). This is supported by plotting the muscovite analyses on the discrimination diagram of Miller [et al. \(1981\)](#); they fall in the field of primary muscovite (**Fig. 5e**).

The amphiboles are only analyzed in the alkaline and peralkaline granites of ARC. The chemical formulae were calculated on the basis of 23 oxygen atoms in the anhydrous total and are represented in Supplementary Table 9S. The 13-CNK method of Leake [et al. \(1997\)](#) is used to calculate the ferrous and ferric iron of the analyzed amphiboles. Using the classification scheme of Leake [et al. \(1997\)](#), the analyzed amphiboles are Na-rich and classified as alkali amphiboles (**Fig. 5f**). The analyzed alkali amphiboles have $(\text{Na}+\text{K})_{\text{A}} > 0.5$ and are represented mainly by arfvedsonite with minor ferro-eckermannite (see Supplementary Table 9S). All the analyzed sodic amphiboles contain >0.1 Ti p.f.u., a characteristic of primary igneous amphiboles ([Girardeau and Mevel 1982](#)).

6. Whole rock geochemistry

6.1. Geochemical characteristics

The chemical analyses of the ARC granites and MMEs, as well as their calculated normative mineral compositions and rare-earth elements contents, are listed in Tables 1–3. The granitic rocks cover a wide range of compositions (68.97–75.27 wt.% SiO₂), differentiation indices (DI = 82–91), and total alkalis (Na₂O+K₂O = 8.63–9.68 wt.%). The chemical composition of monzogranite is less evolved than other granitic rocks of the ARC, with SiO₂ contents ranging from 68.97 to 70.44 wt.%. It has high Al₂O₃, TiO₂, Fe₂O₃, CaO, MgO, Ba, and Sr, but contains less total alkali content, Rb, Nb, Y, Zr, and Th. The granophyre has chemical composition overlaps with the syenogranite and alkali feldspar granite. The alkali feldspar granite and alkaline/peralkaline granite show limited variation in their compositions and they are similar in most major and trace element contents. The granitic rocks of the ARC are conspicuously depleted in Ba (average = 80 ppm) and Sr (average = 27 ppm), and have high concentrations of Nb (94 ppm), Y (105 ppm), Zr (965 ppm), and Th (26 ppm), which are similar to the alkaline/peralkaline granites in the ANS (e.g., [Katzir et al. 2007](#); [El-Bialy and Streck 2009](#); [Khalil et al. 2018](#)). According to the R₁–R₂ classification diagram of [De la Roche et al. \(1980\)](#), the ARC granites appear in the alkali granite field (**Fig. 6**), which are characteristic of all alkaline and peralkaline rocks. This classification is supported by the abundance of orthoclase and albite in the normative composition (Table 2).

Selected major and trace elements of the ARC granites are plotted against SiO₂ and used as a differentiation index (**Figs. 7, 8**). The studied granitic rocks show continuous trends with most major and trace elements, without any compositional gap between them. The major oxides

show relatively smooth variation with gradual decreases in TiO₂, Fe₂O₃, MnO, MgO, and CaO 367
with increasing SiO₂ content, whereas K₂O increases. Regarding the trace elements, Nb, Y, Rb, 368
Ta, Th Zr, and Hf increase, whereas Sr, Ba, V, Ni, and Sc decrease with increasing of SiO₂ 369
content. 370

The spider diagrams, using the MORB normalization values of Pearce (1983), for the 371
averages of the ARC granites are shown in **Fig. 9a**. It is clear that the granitic samples show 372
general similarities in their patterns. They are enriched in some large ion-lithophile elements 373
(LILEs) (Rb, K, Th) and high field strength elements (HFSEs) (Ta, Zr, Hf), but strongly depleted 374
in Ba, Sr, P, and Ti, which is consistent with the geochemical signature of A-type granite ([Jahn](#) 375
[et al. 2001](#); [Wu et al. 2002](#)). 376

The concentrations of rare-earth elements (REEs), together with some statistical 377
parameters, are listed in Table 3. The chondrite-normalized REE patterns for the averages of the 378
ARC granites are presented in **Fig. 9b**. The ARC granites show wide variation in REE contents 379
that depend, most probably, on the nature of the crystallizing accessory mineral phases. They are 380
rich in light rare-earth elements (LREEs) relative to heavy rare-earth elements (HREEs). The 381
monzogranite samples have the lowest concentrations of REEs (180–273ppm, average 222 ppm), 382
and the peralkaline granite has the highest contents of REEs (1102–1579 ppm, average 1319 383
ppm). The granophyre samples show clear overlap in their HREEs with the alkali feldspar 384
granite and alkaline granite. 385

The Eu/Eu* values range from 0.21 to 0.22 in monzogranite, 0.14–0.25 in syenogranite, 386
0.17–0.23 in granophyre, 0.17–0.22 in alkali feldspar granite, 0.11–0.17 in alkaline granite, and 387
0.12–0.17 in peralkaline granite (**Fig. 9**). The strongly negative Eu/Eu* anomalies (0.11–0.25) 388
associated with very low Ba and Sr concentrations indicate extreme feldspar fractionation 389

(Hanson 1980; Möller and Muecke 1984; Lee et al. 2013). Additionally, the very low Eu/Eu* in the ARC granites can attribute to melt–fluid interaction at the end stage of magma evolution (Irber 1999; Jahn et al. 2001; Zhao et al. 2002).

The MMEs have a limited composition range with respect to their silica contents (57.16–58.54 SiO₂ wt.%). On the R₁–R₂ classification diagram of De la Roche et al. (1980), they appear within the diorite field (**Fig. 6**). The spider diagrams, using the MORB normalization values of Pearce (1983), for the MMEs are shown in **Fig. 9c**. They show strong similarities in the spider diagrams, with greater enrichment in the LILEs than the HFSEs. Additionally, the normalized patterns of the MMEs have Nb-Ta depletion similar to volcanic-arc rocks (Saunders et al., 1980; Hollings and Wyman, 1999). The chondrite-normalized REE patterns of the MMEs, using the C1-chondrite normalization values of Evensen et al. (1978), are represented in **Fig. 9d**. They are enriched in LREEs relative to HREEs [(La/Yb)_n = 12.92–14.51] with slightly positive Eu-anomalies [(Eu/Eu*)_n = 1.03–1.16] due to plagioclase accumulation.

6.2. Magma type and tectonic setting

On the ANK vs. ACNK diagram (**Fig. 10a**) of Maniar and Piccoli (1989), the ARC granites are mainly peralkaline in character. This is proved by the normative acmite (1.79–3.23) and Na-metasilicate (0.25–3.39) in their norms (Table 2). The agpaitic indexes [AI = molar ((Na+K)/Al)] of the studied granites are high (1.06–1.37) characteristics for alkaline/peralkaline A-type rocks (Liégeois and Black 1987; Liégeois et al. 1998). The alkaline/peralkaline character of ARC granites are confirmed by using the diagram of Sylvester (1989), which is used to distinguish between granitic rocks with SiO₂ > 68 wt.% (**Fig. 10b**). Additionally, the presence of both sodic amphibole and sodic pyroxene support the alkaline/peralkaline nature of the studied

granitic rocks. [Whalen et al. \(1987\)](#) used plots of Ga/Al versus certain major and trace elements (Fig. 10c) to discriminate between A-type granites and other granites (M-, I-, and S-type granites). The studied A-type granites of the ARC have 10000*Ga/Al ratios (>2.5) higher than the average values of 2.28 and 2.10 for S- and I-type granites, respectively ([Whalen et al. 1987](#)). On the 10000*Ga/Al vs. FeO/MgO diagram, the granitic samples of the ARC appear in the A-type granite field (Fig. 10c). The agpaitic indexes of the investigated MMEs are less than 0.87 (0.55–0.58), which is similar to calc-alkaline rocks ([Liégeois and Black 1987](#); [Liégeois et al. 1998](#)). On the discrimination diagram of [Maniar and Piccoli \(1989\)](#), they appear in the metaluminous field (Fig. 10a).

The overall chemical characteristics of the studied granites are consistent with a within-plate tectonic setting. They have alkaline/peralkaline characters and remarkable depletion in CaO, MgO, Sr, and transition metals, as well as high contents of alkalis. Moreover, they have marked enrichment in HFSEs including REEs, with pronounced negative Eu anomalies. These geochemical features are typically characteristic of within-plate magmatism ([Whalen et al. 1987](#); [Eby 1990, 1992](#)). The within-plate tectonic setting of the studied granites is substantiated by plotting the trace element data on suitable discrimination diagrams. Using the Rb vs. Y+Nb tectonic discrimination ternary diagram of [Pearce et al. \(1984\)](#), the ARC granites appear in the within-plate field (Fig. 10d). The Rb-Hf-Ta discrimination diagram of [Harris et al. \(1986\)](#) confirms the within-plate tectonic setting (Fig. 10e). On the multicationic diagram of [Batchelor and Bowden \(1985\)](#), the ARC samples appear in the anorogenic to post-orogenic granitic fields (Fig. 10f). The MMEs are plotted on the volcanic-arc tectonic setting (Fig. 10 d, e, f).

The geochemical characteristics of certain mafic minerals in igneous rocks may be used to identify the original magmatic affinity and may be directly employed in deducing the tectonic

environments of their host magmas (e.g., Cameron and Papike 1981; S Nachit et al. 1985; Smith and Brown 1988; Abdel-Rahman 1994). The composition of pyroxene, amphibole, and biotite in the ARC granites can furnish, to some extent, criteria to deduce their tectono-magmatic affiliation that can confirm the inferences from whole-rock geochemistry. The presence of sodic amphiboles in the ARC indicates their peralkaline tendency (Middlemost 1997). The composition of biotites indicates the nature of the original parent magma (Nachit et al. 1985; Abdel-Rahman 1994). On the biotite discrimination diagrams (Figs. 5c, d), the analyzed biotite crystals from both the monzogranite and syenogranite appear in the field of the alkaline anorogenic suite, and show virtually no overlap with other fields, indicating their chemically distinct nature.

7. Petrogenesis

7.1. Petrogenetic source of the Aja Ring Complex

Many petrogenetic models have been proposed for the formation of the A-type rocks of the ANS (Katzir et al. 2007; Eyal et al. 2010; Boskabadi et al. 2013; Azer et al. 2014; Sami et al. 2017, 2018; Khalil et al. 2018), but no single model has been suggested that satisfactorily explains all the variations their chemical compositions. In fact, the large differences in isotope ratios as well as major and trace element concentrations among the various A-type granitic rocks of the ANS strongly suggest that they originated from a variety of processes and sources. The suggested models for the generation of the A-type rocks of the ANS include the (1) fractional crystallization of mafic magma derived from mantle (e.g., Stern and Voegeli 1987; Beyth et al. 1994; Mushkin et al. 2003; Jarrar et al. 2008), (2) partial melting of various pre-existing crustal rocks (e.g., Abdel-Rahman 2006; Farahat et al. 2007; Ali et al. 2009; Eyal et al. 2010; Sherif et

al. 2013), and (3) combination of a mantle source with crustal materials (e.g., Azer 2006; Samuel 459
et al. 2007; Be’eri-Shlevin et al. 2009; Ali et al. 2015; Khalil et al. 2018). 460

The interpretations of the genesis of the ARC in particular are diverse and pioneering 461
works have caused many controversies (Stuckless et al. 1984; Ekren et al. 1987; Qadhi 2007; 462
Herrher and Abdallah 2017). The present field work reported much evidence regarding the 463
sequence of intrusion of the ARC, which indicates its emplacement within two phases. However, 464
the presence of both gradational and sharp contacts between the two phases suggests that they 465
were emplaced within a very short time interval, before the complete crystallization of the first 466
phase. The absence of geochemical compositional gaps in most major and trace elements in the 467
ARC granites, with continuous evolutionary trends of compatible and incompatible elements, 468
suggest their derivation from a common source. 469

The ARC shares many features of highly fractionated A-type granite, including high 470
concentrations of Rb (135–318 ppm), Nb (67–137 ppm), Y (54–176 ppm), Zr (404–1660 ppm), 471
and Ta (4–10 ppm) but low concentrations of Ba (16–161 ppm) and Sr (9–57 ppm). The 472
geological setting and the geochemical data of the ARC granites indicate they were emplaced in 473
post-collisional within-plate tectonic setting. According to the discrimination diagram of Eby 474
(1990), the granites of the ARC appear in the A₁ field on the Rb/Nb vs. Y/Nb diagram (**Fig.** 475
11a). Accordingly, the studied A-type granites were derived through the partial melting of pre- 476
existing crustal rocks with a mantle contribution. Khalil et al. (2018) attributed the “mantle” 477
signature in the A-type granites in the ANS to the partial melting of juvenile continental crust. 478
Recent published studies indicate that isotopic data from the juvenile crust of the ANS cannot 479
distinguish between lower crust and upper mantle, because the radiogenic isotope ratios of both 480

sources in the ANS are similar (e.g., [Stern and Gottfried 1986](#); [Stern 2002](#); [Hargrove et al. 2006](#); [Eyal et al. 2010](#); [Morag et al. 2011](#); [Moreno et al. 2014](#); [Eyal et al. 2014](#)).

The absence of mafic lithologies in the ARC argues against the extensive fractional crystallization of mantle-derived mafic magma. This is supported by low values of Mg# (2–7, Table 1) and low concentrations of Co (3–9 ppm), Ni (1–3 ppm), V (2–5 ppm), and Sc (1–3 ppm). Additionally, it is difficult to explain the great quantities of felsic rocks in the ARC, which cannot result from the fractional crystallization of mafic magma. Many geological, geochemical, and isotopic characteristics of the A-type rocks of the ANS argue against a mantle source (e.g., [Abdel-Rahman 2006](#); [Eyal et al. 2010](#); [Ali et al. 2009](#); [Eyal et al. 2010](#)). Additionally, certain ratios of the highly incompatible trace elements (e.g., Zr/Nb, Ba/Nb, Rb/Nb and K/Nb; Table 1) have averages lying within or near the values of the continental crust ([Weaver 1991](#); [Wedepohl 1994](#)).

The ARC was most probably generated via the partial melting of a juvenile crustal source, followed by extensive fractional crystallization. The presence of MMEs and xenoliths indicate mixing between two magmas and contamination with crustal rocks. Among potential crustal sources for the parental melt of the ARC include the Neoproterozoic upper crustal rocks such as schists, gneisses, metagabbro-diorite, and I-type calc-alkaline granitoids. The presence of gneiss xenoliths within the early phase of the ARC support its derivation through the partial melting of a juvenile crustal source. This is supported by the experimental works that indicate the dehydration melting of calc-alkaline tonalite at 950 °C and 0.4 GPa can produce melts with major and trace element characteristics of A-type magmas (e.g., [Patino Douce 1997](#)).

The suggested model for the evolution of A-type rocks of the ARC is shown in **Fig. 11b**. At the first stage, mantle-derived magma is produced as a result of lithospheric extension, which

leads to the asthenospheric upraise, causing extensive melting of some parts of the lithosphere. 504
 Additionally, the lithospheric extension pressure will release at depth, causing an influx of 505
 volatiles in the crust from deeper sources. A mantle-derived volatile phase brings additional heat, 506
 which is necessary to decrease the melting temperature of rocks and initiate partial melting 507
 (Bailey 1974). Shear zones and intra-continental large-scale faults facilitate the produced magma 508
 to enter the overlying middle and upper crusts, and promote the partial melting process. Then, 509
 the mingling and mixing of magmas produces magmatism with an intermediate composition that 510
 could evolve to felsic magmatism with granitic composition. The emplacement of the ARC most 511
 probably occurred after the termination of the Pan-African orogeny, along with re-activated Pan- 512
 African fractures. The dyke swarms that cut the early phase of the ARC support an extensional 513
 tectonic regime during the emplacement of the studied A-type granites. The proposed 514
 geotectonic model for the generation of the ARC is similar to the lithospheric delamination 515
 model suggested by many authors for the evolution of the post-collisional alkaline/peralkaline 516
 phase in the ANS (e.g., [Avigade and Gvirtzman 2009](#); [Farahat and Azer 2011](#); [Khalil et al. 2018](#)). 517
 518

7.2. Fractional crystallization and crustal contamination 520

The present geochemical data including variation diagrams of major and trace elements 521
 (Figs. 7, 8) and the continuity of normalized trace element and REE patterns (Fig. 9a, b) are 522
 consistent with evolution through magmatic differentiation from a common parental magma. The 523
 main fractionated phases include feldspars with minor roles of mafic minerals, apatite, and Fe-Ti 524
 oxides. The fractionation of feldspars is indicated by the systematic decrease in Sr and Ba from 525
 monzogranite to peralkaline granite (Fig. 12a) and by the plot of Sr vs. Rb/Sr (Fig. 12b). The 526

increasing K₂O with increasing SiO₂ through the granitic rocks of the ARC argues against 527
removal of the abundant alkali feldspar as a fractionating phase, whereas decreasing CaO and 528
Na₂O with increasing SiO₂ are consistent with plagioclase fractionation, although plagioclase is a 529
minor or absent phase in the ARC granites. The multi-element spider diagrams of the averages of 530
the ARC granites (**Fig. 9a**) show negative anomalies for Ba, Sr, Ti, and P that can be attributed 531
to feldspars, Fe-Ti oxides, and apatite, respectively. The strongly fractionated nature of the REE 532
patterns of the ARC granites (**Fig. 9b**) and, in particular, the pronounced negative Eu anomalies 533
(Eu/Eu* = 0.12–0.25) provide strong evidence for the extensive fractional crystallization of 534
feldspars from a parental magma at depth before the emplacement of the earliest exposed phase 535
(monzogranite) under reducing conditions to stabilize Eu²⁺ ([Hanson 1978](#); [McKay 1989](#); [Khalil 536](#)
[et al. 2018](#)). This is supported by the strong depletion in Ba (av. 80 ppm) and Sr (av. 27 ppm). 537
Systematic decreases in MgO and Fe₂O₃ and with increasing silica (**Fig. 7**) suggest the extraction 538
of primary mafic minerals followed by Fe-Ti oxide fractionation. 539

On the Rb versus K/Rb diagram (**Fig. 12c**), all the ARC granites follow the trend of 540
fractional crystallization and assimilation ([Akinin et al. 2009](#); [Miller and Snoke 2009](#)). This 541
indicates that both fractional crystallization and crustal contamination played roles during the 542
evolution of the ARC. The presence of MMEs in the early phase of the ARC indicates the 543
mingling of diverse magmas, whereas the presence of gneiss xenoliths indicates the assimilation 544
of the host rocks. The MMEs represent cooled globules from a basic magma that mixed with the 545
partly crystalline granitic magma. The granitic rocks of the ARC show wide variations in certain 546
ratios such as K/Rb, Ba/Nb, and Zr/Rb (Table 1), reflecting the role of crustal contamination 547
during fractional crystallization. The constant values of these ratios point instead to simple 548
fractional crystallization ([Davidson et al. 1988](#)). 549

7.3. Crystallization conditions

The present study indicates that the ARC was emplaced at shallow crustal levels, which is supported by the association of coeval plutonic and volcanic rocks and the presence of miarolitic cavities as well as granophyric intergrowths. Most of the granitic rocks of the ARC have a hypersolvus nature that indicates high temperatures of crystallization and low water pressure, similar in this regard to other alkaline rocks emplaced at relatively shallow depth (King et al. 1997; Klimm et al. 2003; Azer 2013; Khalil et al. 2018). The presence of fluorite in the ARC granites indicates that magma was fluorine-rich, which affected the physicochemical properties of granitic magma. This could lower the viscosity of the melts and the crystallization temperature of granitic magmas, leading to faster migration of melts and emplacement at shallow levels (Dingwell 1985, 1988; Hannah and Stein 1990; Azer 2013; Khalil et al. 2018).

The ARC granites are characterized by the presence of graphic intergrowth between quartz and feldspars. The formation of graphic texture may be promoted by the presence of fluorine, which decreases water solubility in the melt and increases the abundance of the exsolved vapor phase. The genesis of graphic texture has been variously attributed to the replacement of the host mineral by a guest mineral or to the eutectic crystallization of intergrowth-forming minerals (Khalil et al. 2018). The absence of clear evidence for the replacement of feldspars by quartz indicates the eutectic crystallization of intergrowth-forming minerals.

8. Conclusions

- The ARC represents the youngest phase of late Neoproterozoic igneous activity in the 572
northeastern part of the Arabian Shield, which resulted in the emplacement of a great number 573
of A-type igneous intrusions. 574
- The ARC is undeformed and unmetamorphosed, and was emplaced as a ring-shaped pluton. 575
Two granitic phases of the ARC are distinguished; the earlier phase includes monzogranite, 576
syenogranite, granophyre, and alkali feldspar granite, intruded by the younger second phase 577
consisting of alkaline and peralkaline granites. The contacts between the different granitic 578
rocks of the ARC are gradational to sharp contacts, suggesting their emplacement within a 579
very short time interval, before the complete crystallization of the early phase. 580
- The ARC granites have a hypersolvus nature, suggesting a shallow depth of emplacement, 581
low water pressure, and high temperature of crystallization. The granite samples of the ARC 582
host numerous accessory minerals and share many features of rare-metal bearing granites. 583
The presence of sodic pyroxene and sodic amphibole indicate the peralkaline affinity of the 584
ARC. The ARC was emplaced in the shallow crust level during the post-collisional phase of 585
the ANS assembly. The ARC granites display general characteristics of A-type rocks and are 586
classified as mineralized granites. 587
- The overall major and trace element trends and elemental ratios, as well as the increasingly 588
fractionated nature of the REE patterns, suggest that the ARC granites represent one 589
cogenetic suite. They were derived from a crustal source that underwent magmatic 590
differentiation and crustal contamination. The main fractionated phase involves feldspars 591
with minor roles for the fractionation of amphibole, biotite, apatite, and Fe-Ti oxides. The 592
contamination with crustal materials is indicated by MMEs, mafic xenoliths, and trace- 593
element ratios. 594

- Lithospheric delamination below the ANS was an upwelling of hot asthenosphere and melting the lithospheric mantle, producing basaltic melts below the crust that provide heat for the partial melting of the lower crust.

Acknowledgment

The author would like to extend his appreciation and gratefulness to the Deanship of Scientific Research and RSSU at King Saud University for funding and supporting this work through Research Group Number RG-1439-037. In addition, the author convey his heartily appreciation and grateful for the editor (Prof. David B. Rowley) for his time and effort, besides for his comprehensive comments and remarks. Furthermore, the author very appreciative and grateful for the anonymous reviewer.

References

- Abdel-Rahman, A.M. 1994. Nature of biotites from alkaline, calc-alkaline and peraluminous magmas. *J. Petrol.* 35: 525–541.
- Abdel-Rahman, A.M. 2006. Petrogenesis of anorogenic peralkaline granitic complexes from eastern Egypt. *Mineral. Mag.* 70: 27–50.
- Akinin, V.V.; Miller, E.L. and Wooden, J.L. 2009. Petrology and geochronology of crustal xenoliths from the Bering Strait Region: Linking deep and shallow processes in extending continental crust. *Geol. Soc. Am. Special Paper* 456.
- Ali, K.A.; Azer, M.K.; Gahlan, H.A.; Wilde, S.A.; Samuel, M.D. and Stern, R.J. 2010. Age constraints on the formation and emplacement of Neoproterozoic ophiolites along the Allaqi-Heiani suture, South Eastern Desert of Egypt. *Gondwana. Res.* 18: 583–595.
- Ali, B.H.; Wilde, S.A. and Gabr. M.M.A. 2009. Granitoid evolution in Sinai, Egypt, based on precise SHRIMP U-Pb zircon geochronology. *Gondwana. Res.* 15: 38–48.

- Ali, K.A.; Surour; A.A.; Whitehouse, M.J. and Andresen, A. 2015. Single zircon Hf–O isotope constraints on the origin of A-type granites from the Jabal Al-Hassir ring complex, Saudi Arabia. *Precambrian. Res.* 256: 131–147.
- Ali, K.A.; Jeon, H.; Li, A.; Andresen, S.-Q.; Harbi, H.M. and Hegner, E. 2014. U–Pb zircon geochronology and Nd–Hf–O isotopic systematics of the Neoproterozoic Haddadh Dayheen ring complex, Central Arabian Shield, Saudi Arabia. *Lithos* 206–207: 348–360.
- Avigad, D. and Gvirtzman, Z. 2009. Late Neoproterozoic rise and fall of the northern Arabian-Nubian shield: The role of lithospheric mantle delamination and subsequent thermal subsidence. *Tectonophysics* 477: 217–228.
- Azer, M.K.; Obeid, M.A. and Ren, M. 2014. Geochemistry and petrogenesis of late Ediacaran (580-605 Ma) post-collisional alkaline rocks from Katherina Ring complex, south Sinai., Egypt. *J. Asian Earth Sci.* 93: 229–252.
- Azer, M.K. 2006. The petrogenesis of late Precambrian felsic alkaline magmatism in South Sinai, Egypt. *Acta. Geol. Polon.* 56: 463–484.
- Azer, M.K. 2013. Late Ediacaran (605-580 Ma) post-collisional alkaline magmatism in the Arabian–Nubian Shield: a case study of Serbal ring-shaped intrusion, southern Sinai, Egypt. *J. Asian Earth Sci.* 77: 203–223.
- Azer, M.K.; Gahlan, H.A.; Asimow, P.D. and Al-Kahtany, K.M. 2017. The Late Neoproterozoic Dahanib mafic-ultramafic intrusion, South Eastern Desert, Egypt: is it an Alaskan-type or a layered intrusion? *Am. J. Sci.* 317: 901–940.
- Bailey, D.K. 1974. Origin of alkaline magmas as a result of anatexis, (b) crustal anatexis. In: Sorenson, H. (ed.), *The alkaline rocks*. Wiley & Sons, London, 436–442.

- Basta, F.F.; Maurice, A.E.; Betros, B.R.; Azer, M.K. and El-Sobky, A., 2017. Intrusive Rocks of the Wadi Hamad Area, North Eastern Desert, Egypt: Change of Magma Composition with Maturity of Neoproterozoic Continental Island Arc and the Role of Collisional Plutonism in the Differentiation of Arc Crust. *Lithos* 288–289: 248–263.
- Batchelor, R.A. and Bowden, P. 1985. Petrogenetic interpretation of granitoid rock series, using multicationic parameters. *Chem. Geol.* 48: 43–45.
- Be’eri-Shlevin, Y.; Katzir, Y., Whitehouse M., 2009. Post-collisional tectono-magmatic evolution in the northern Arabian-Nubian Shield (ANS): Time constraints from ion-probe U-Pb dating of zircon. *J. Geol. Soc. London* 166: 71–85.
- Beyth, M.; Stern, R.J.; Altherr, R. and Kröner, A. 1994. The late Precambrian Timna igneous complex Southern Israel: Evidence for comagmatic-type sanukitoid monzodiorite and alkali granite magma. *Lithos* 31: 103–124.
- Boskabadi, A.; Pitcairn, I.K.; Stern, R.J.; Azer, M.K.; Broman, C.; Mohamed, F.H. and Majka, J. 2013. Carbonatite crystallization and alteration in the Tarr carbonatite-albitite complex, Sinai Peninsula, Egypt. *Precambrian Res.* 239: 24–41.
- Davidson, J.P.; Dungan, M.A.; Ferguson, K.M. and Colucci, M.T., 1988. Crust-magma interactions and the evolution of arc magmas: the San Pedro-Pellado Volcanic Complex Southern Chilean Andes. *Geol.* 15: 443–446.
- De la Roche, H.; Leterrier, J.; Grandclaude, P. and Marchal, M., 1980. A classification of volcanic and plutonic rocks using R_1 - R_2 diagrams and major-element analyses—Its relationship with current nomenclature. *Chem. Geol.* 29: 183–210.
- Dingwell, D.B. 1985. The structure and properties of fluorine-rich silicate melts: implications for granite petrogenesis. In R.P. Taylor and D.F. Strong (eds.), *Granite-related mineral*

- deposits geology, petrogenesis and tectonic setting, CIM Conference on Granite-related Mineral Deposits, 72–81. 665 666
- Drysdall, A.R. and Douch, C.J. 1986. Nb–Th–Zr mineralization in microgranite – microsyenite at Jabal Tawlah, Midyan region, Kingdom of Saudi Arabia. *J. Afr. Earth Sci.* 4: 275–288. 667 668
- Drysdall, A.R.; Jackson, N.J.; Douch, C.J.; Ramsay, C.R. and Hackett, D., 1984. Rare metal mineralization related to alkali granites in the Arabian Shield. *Econ. Geol.* 79: 1366–1377. 669 670 671
- Eby, G.N. 1990. The A-type granitoids: A review of their occurrence and chemical characteristics and speculations on their petrogenesis. *Lithos* 26: 115–134. 672 673
- Eby, G.N. 1992. Chemical subdivisions of the A-type granitoids: petrogenesis and tectonic implications. *Geol* 20: 641–644. 674 675
- Ekren, E.B.; Vaslet, D.; Berthiaux, A.; Strat, P. L. and Fourniguet, J. 1987. Geologic map of the Ha'il Quadrangle, Sheet 27E, Kingdom of Saudi Arabia, Deputy Ministry for Mineral Resources, Ministry of Petroleum and Mineral Resources, Kingdom of Saudi Arabia, Scale 1: 250,000. 676 677 678 679
- El-Bialy, M.Z. and Streck, M.J. 2009. Late Neoproterozoic alkaline magmatism in the Arabian–Nubian Shield: the Post-Collisional A-type granite of Sahara-Umm Adawi pluton, Sinai, Egypt. *Arab. J. Geosci.* 2: 151–174. 680 681 682
- Elliott, J.E.; Al-Yazidi, S.; Al-Eissa, H.; Al-Shammeri, A.; Hashem, H.I. and Tarabulsi, Y. 1999. Exploration of the Ghurayyah Radioactive Granite, Kingdom of Saudi Arabia. Saudi Geological Survey Technical Report, Open-File Report. 683 684 685
- Evensen, N.M.; Hamilton, P.J. and O' Nions, R.K. 1978. Rare earth abundances in chondritic meteorites. *Geochim. Cosmochim. Acta.* 42: 1199–1212. 686 687

- Eyal, M.; Litvinovsky, B.; Jahn, B.M.; Zanvilevich, A. and Katzir Y. 2010. Origin and evolution of post-collisional magmatism: Coeval Neoproterozoic calc-alkaline and alkaline suites of the Sinai Peninsula. *Chem. Geol.* 269: 153–179.
- Eyal, M.; Zanvilevich, A.N.; Litvinovsky, B.A.; Jahn, B.M.; Vapnik, Ye. and Be'eri-Shlevin, Y. 2014. The Katherina ring complex (Sinai Peninsula, Egypt): Sequence of emplacement and petrogenesis. *Am. J. Sci.* 314: 462–507.
- Farahat, E.S. and Azer, M.K. 2011. Post-collisional magmatism in the northern Arabian-Nubian Shield: the geotectonic evolution of the alkaline suite at Gebel Tarbush area, south Sinai, Egypt. *Chem. Erde-. Geochem.* 71: 247–266.
- Farahat, E.S.; Mohamed, H.A.; Ahmed, A.F. and El Mahallawi, M.M. 2007. Origin of I- and A-type granitoids from the Eastern Desert of Egypt: implications for crustal growth in the northern Arabian–Nubian Shield. *J. Afr. Earth Sci.* 49: 43–58.
- Farahat, E.S.; Zaki, R.; Hauzenberger, C., and Sami, M. 2011. Neoproterozoic calc-alkaline peraluminous granitoids of the Deleihimmi pluton, Central Eastern Desert, Egypt: implications for transition from late- to post-collisional tectonomagmatic evolution in the northern Arabian–Nubian Shield. *Geol. J.* 46: 544–560.
- Gahlan, H.A.; Azer, M.K.; Asimow, P.D. and Al-Kahtany, K. 2016. Late Ediacaran post-collisional A-type syenites with shoshonitic affinities, northern Arabian-Nubian Shield: A possible mantle-derived A-type magma. *Arab. J. Geosci.* 9: 613([doi:10.1007/s12517-016-2629-x](https://doi.org/10.1007/s12517-016-2629-x)).
- Genna, A.; Nehlig, P.; Le Goff, E.; Gguerrot, Cc and Shanti, M. 2002. Proterozoic tectonism of the Arabian Shield. *Precambrian Res.* 117: 21–40.

Girardeau, J. and Mevel, C. 1982. Amphibolitized sheared gabbros from ophiolites as indicators	710
of the evolution of the oceanic crust: Bay of islands, Newfoundland. <i>Earth Planet. Sc.</i>	711
<i>Lett.</i> 61:151–165.	712
Hackett, D. 1986. Mineralized aplite–pegmatite at Jabal Sa'id, Hijaz region, Kingdom of Saudi	713
Arabia. <i>J. Afr. Earth Sci.</i> 4: 257–267.	714
Hannah, J.L. and Stein, H.J. 1990. Magmatic and hydrothermal processes in ore bearing systems.	715
In Stein HJ and Hannah JL (eds) <i>Ore-bearing granite systems; petrogenesis and</i>	716
<i>mineralizing processes. Geol. Soc. Am. Special Paper</i> , 246:1–10.	717
Hanson, G.N. 1978. The application of trace elements to the petrogenesis of igneous rocks of	718
granitic composition. <i>Earth Planet. Sc. Lett.</i> 38: 26–43.	719
Hanson, G.N. 1980. Rare earth elements in petrogenetic studies of igneous systems. <i>Ann. Rev.</i>	720
<i>Earth Planet. Sci.</i> 8: 371–406.	721
Hargrove, U.S.; Stern, R.J.; Kimura, J.-I.; Manton, W.I. and Johnson, P.R. 2006. How juvenile is	722
the Arabian-Nubian Shield? Evidence from Nd isotopes and pre-Neoproterozoic inherited	723
zircon in Bi'r Umk suture zone, Saudi Arabia. <i>Earth Planet. Sc. Lett.</i> 252: 308–326.	724
Harrher, M.E. and Abdullah S. E. 2017. Lithologic mapping of Aja granitic batholiths, Ha'il,	725
Saudi Arabia, using remote sensing. <i>Arab. J. Geosci.</i> 10: 313.	726
Harris, N.B.W. 1985. Alkaline complexes from the Arabian Shield. <i>J. Afr. Earth Sci.</i> 3:83–88.	727
Harris, N.B.W.; Pearce, J.A. and Tindle, A.G. 1986. Geochemical characteristics of collision-	728
zone magmatism. In: Coward MP and Ries AC (eds) <i>Collision tectonics. J. Geol. Soc.</i>	729
London, Special Publication 19: 67–81.	730

Hollings, P. and Wyman, D. 1999. Trace element and Sm-Nd systematics of volcanic and
intrusive rocks from the 3 Ga Lumby Lake Greenstone Belt, Superior Province: evidence
for Archean plume-arc interaction. *Lithos* 46: 189–213.

Irber, W. 1999. The lanthanide tetrad effect and its correlation with K/Rb, Eu/Eu*, Sr/Eu, Y/Ho,
and Zr/Hf of evolving peraluminous granite suites. *Geochim. Cosmochim. Acta.* 63: 89–
508.

Jackson, N.J. 1986. Petrogenesis and evolution of Arabian felsic plutonic rocks.

Jackson, N.J. and Douch, C.J. 1986. Jabal Hamra REE-mineralized silexite, Hijaz region,
Kingdom of Saudi Arabia. *J. Afr. Earth Sci.* 4: 269–274.

Jahn, B.-M.; Wu, F.Y.; Capdevila, R.; Martineau, F.; Zhao, Z. and Wang, Y. 2001. Highly
evolved juvenile granites with tetrad REE patterns: the Woduhe and Baerzhe granite from
the Great Xing'an Mountains in NE China. *Lithos* 59: 171–198.

Jarrar, G.H.; Manton, W.I.; Stern, R.J. and Zachmann F. 2008. Late Neoproterozoic A-type
granites in the northernmost Arabian-Nubian Shield formed by fractionation of basaltic
melts. *Chem. Erde- Geochem.* 68: 295–312.

Johnson, P.R. 2003. Post-amalgamation basins of the NE Arabian shield and implications for
Neoproterozoic III tectonism in the northern East African orogen. *Precambrian Res.* 123:
321–338.

Johnson, P.R. and Woldehaimanot, B. 2003. Development of the Arabian–Nubian Shield:
perspectives on accretion and deformation in the northern East African Orogen and the
assembly of Gondwana. In: Yoshida M, Dasgupta S, Windley B (eds), *Proterozoic East
Gondwana: supercontinent assembly and breakup*: Geol Soc, London, Special
Publications, 206, pp. 289–325.

- Katzir, Y.; Eyal, M.; Litvinovsky, B.A.; Jahn, B.M.; Zanilevich, A.N.; Valley, J.W.; Beerli, Y. 754
and Shimshilashvili, E. 2007. Petrogenesis of A-type granites and origin of vertical 755
zoning in the Katharina pluton, Gebel Mussa (Mt. Moses) area, Sinai, Egypt. *Lithos* 95: 756
208–228. 757
- Khalil, A.E.S.; Obeid, M.A.; Azer, M.K. and Asimow, P.D. 2018. Geochemistry and 758
petrogenesis of post-collisional alkaline and peralkaline granites of the Arabian-Nubian 759
Shield: a case study from the southern tip of Sinai Peninsula, Egypt. *Int. Geol. Rev.* 60: 760
98–1018. 761
- King, P.L.; White, A.J.R.; Chappel, B.W. and Allen, C.M. 1997. Characterization and origin of 762
aluminous A-type granites from the Lachlan Fold Belt, southeastern Australia. *J. Petrol.* 763
38: 371–391. 764
- Klimm, K.; Holtz, F.; Johannes, W. and King, P.L. 2003. Fractionation of metaluminous A-type 765
granites: an experimental study of the Wangrah Suite, Lachlan Fold Belt, Australia. 766
Precambrian Res. 124: 327–341. 767
- Küster, D. 2009. Granitoid-hosted Ta mineralization in the Arabian–Nubian Shield: ore deposit 768
types, tectono-metallogenic setting, and petrogenetic framework. *Ore Geol. Rev.* 35: 769
68–86. 770
- Leake, B.E.; Wolly, A.R.; Arps, C.E.S.; Birch, W.D.; Gilbert, M.C.; Grice, J.D.; Hawthorne, 771
F.C.; Kato, A.; Kisch, H.J.; Krivovichev, V.G.; Linthout, K.; Laird, J.; Mandarino, J.; 772
Maresch, W.V.; Nickel, E.H.; Rock N.M.S.; Schumacher, J.C.; Smith, D.C.; Stephenson, 773
N.C.N.; Ungaretti, L.; Whitaker, E.J.W. and Youzhi, G. 1997. Nomenclature of 774
amphiboles: report of the subcommittee on amphiboles of the International Mineralogical 775

Association, Commission on new minerals and mineral names. <i>Am. Mineral.</i> 82: 1019–	776
1037.	777
Lee, S.-G.; Asahara, Y.; Tanaka, T.; Lee, S.R. and Lee, T. 2013. Geochemical significance of the	778
Rb–Sr, La–Ce and Sm–Nd isotope systems in A-type rocks with REE tetrad patterns and	779
negative Eu and Ce anomalies: The Cretaceous Muamsa and Weolaksan granites, South	780
Korea. <i>Chem. Erde- Geochem.</i> 73: 75–88.	781
Liégeois, J.P. and Black, R. 1987. Alkaline magmatism subsequent to collision in the Pan-	782
African belt of the Adrar des Iforas. In: Fitton, JG, Upton B.G.J. (eds) <i>Alkaline Igneous</i>	783
<i>Rocks</i> . Geol Soc, Special Publication 30: 381–401.	784
Liégeois, J.P.; Navez, J.; Black, R. and Hertogen, J. 1998. Contrasting origin of post-collision	785
high-K calc-alkaline and shoshonitic versus alkaline and peralkaline granitoids. The use	786
of sliding normalization. <i>Lithos</i> 45: 1–28.	787
Maniar, P.D. and Piccoli, P.M. 1989. Tectonic discrimination of granitoids. <i>Geol Soc Am Bull</i>	788
101:635–643.	789
Matzko, J.J. and Naqvi, M. I. 1978. A summary of niobium and rare earth localities from Ha'il	790
and other areas in western Saudi Arabia-A preliminary study: U.S. Geological Survey	791
Saudi Open-File Report 78-773, (IR)SA-221.	792
Maurice, A.E.; Bakhit, B.R.; Basta, F.F.; Asimow, P.D.; Wälle, M.; Azer, M.K. and El-Sobky,	793
A.F. 2018. The last subduction-related volcanism in the northern tip of the Arabian-	794
Nubian Shield: A Neoproterozoic arc preceding the terminal collision of East and West	795
Gondwana. <i>Precambrian Res.</i> 310: 256–277.	796

- McKay, G.A. 1989. Partitioning of rare earth elements between major silicate minerals and
basaltic melts. In: Lipin BR & McKay GA (eds) Geochemistry and mineralogy of rare
earth elements. Mineral. Soc. Am. 21: 45–77.
- Meert, J.G. 2003. A synopsis of events related to the assembly of eastern Gondwana.
Tectonophysics 362: 1-40.
- Middlemost, E.A.K. 1997. Magmas, rocks and planetary development. A survey of
magma/igneous rock systems. Longman, Harlow, 299 pp.
- Miller, C.F.; Stoddard, E.F.; Bradfish, L.J. and Dollase, W.A. 1981, Composition of plutonic
muscovite: genetic implications: Can. Mineral. 19: 25–34.
- Miller, R.B. and Snoke, A.W. 2009. Crustal cross section from the western north American
cordillera and elsewhere: implications for tectonic and petrologic processes. Geol. Soc.
Am. Special Paper 456.
- Moghazi, A.K.M.; Iaccheri, L.M.; Bakhsh, R.A.; Kotov, A.B. and Ali, K.A. 2015. Sources of
rare-metal-bearing A-type granites from Jabel Sayed complex, Northern Arabian Shield,
Saudi Arabia. J. Asian Earth Sci. 107: 244–258.
- Moghazi , A.M.; Harbi, H.M. and Ali, K.A. 2011. Geochemistry of the Late Neoproterozoic
Hadb adh Dayheen ring complex, Central Arabian Shield: Implications for the origin of
rare-metal-bearing post-orogenic A-type granites. J. Asian Earth Sci. 42: 1324–1340.
- Moghazi, A.M.; Mohamed, F.H. and Kanisawa, S. 1999. Geochemical and petrological evidence
of calc-alkaline and A-type magmatism in the Homrit Waggat and El-Yatima areas of
eastern Egypt. J. Afr. Earth Sci. 29: 535–549.
- Möller, P. and Muecke, G.K. 1984. Significance of Europium anomalies in silicate melts and
crystal-melt equilibria: a re-evaluation. Contrib. Mineral. Petrol. 87: 242–250.

- Morag, N.; Avigad, D.; Gerdes, A.; Belousova, E. and Harlavan, Y. 2011. Crustal evolution and recycling in the northern Arabian-Nubian Shield: New perspectives from zircon Lu–Hf and U–Pb systematics. *Precambrian Res.* 186: 101–116.
- Moreno, J.A.; Molina, J.F.; Montero, P.; Abu Anbar, M.; Scarrow, J.H.; Cambeses, A. and Bea, F. 2014. Unraveling sources of A-type magmas in juvenile continental crust: Constraints from compositionally diverse Ediacaran post-collisional granitoids in the Katerina Ring Complex, southern Sinai, Egypt. *Lithos* 192–195: 56–85.
- Morimoto, N.; Fabries, J.; Ferguson, A.K.; Ginzburg, I.V.; Ross, M.; Seifert, F.A. and Zussman, J. 1988. Nomenclature of pyroxenes. *Mineral. Mag.* 52: 535–550.
- Moufti, M.R.; Hassanen, M.A. and Hashad, M.H. 2002. Geochemistry and petrogenesis of peralkaline–calc alkaline granites from Radwa-Qeshara complex, Arabian Shield. *Ann Geol Survey Egypt XXV*: 225–249.
- Mushkin, A.; Navon, O.; Halicz, L.; Heimann, A.; Hartmann, G. and Stein, M. 2003. The petrogenesis of A-type magmas from the Amram Massif, southern Israel. *J. Petrol.* 44:815–832.
- Nachit, H.; Ibhi, A.; Abia, E.H. and Ohoud, M.B. 2005. Discrimination between primary magmatic biotites, reequilibrated biotites and neoformed biotites. *Comptes Rendus Géoscience* 337: 1415–1420.
- Nachit, H.; Razafimahefa, N.; Stussi, J.M. and Carron, J.P. 1985. Composition chimique des biotites et typologie magmatique des granitoides. *Comptes Rendus Hebdomadaires de L’Academie des sciences* 301: 813–818.
- Patchett, P.J. and Chase, C.G. 2002. Role of transform continental margins in major crustal growth episodes. *Geol.* 30: 39–42.

Patino Douce, A.E. 1997. Generation of metaluminous A-type granites by low-pressure melting	843
of calc-alkaline granitoids. <i>Geol.</i> 25: 743–746.	844
Pearce, J.A. 1983 Role of sub-continental lithosphere in magma genesis at active continental	845
margins. In: Hawkesworth CJ, Norry MJ (eds) <i>Continental Basalts and Mantle Xenoliths</i> .	846
Shiva, Nantwich, UK, pp. 230–249.	847
Pearce, J.A.; Harris, N.B.W. and Tindle, A.G. 1984. Trace element discrimination diagrams for	848
the tectonic interpretation of granitic rocks. <i>J. Petrol.</i> 25: 956–983.	849
Qadhi, T.M. 2007. Geochemical evolution of rare metal-bearing A-type granites from the Aja	850
Batholith, Hail Terrain, Saudi Arabia. <i>J. Geol. Soc. India</i> 70: 714–729.	851
Ramsay, C.R.; Drysdall, A.R. and Clark, M.D. 1986. Felsic plutonic rocks of the Midyan region,	852
Kingdom of Saudi Arabia- II. Pilot study in chemical classification of Arabian granitoids.	853
<i>J. Afr. Earth Sci.</i> 4: 79–85.	854
Richard, L.R. 1995. Mineralogical and petrological data processing system. Minpet Software (c)	855
1988–1995, Version 2.02.	856
Sami, M.; Ntaflos, T.; Farahat, E.S.; Mohamed, H.A.; Hauzenberger, C. and Ahmed, A.F. 2018.	857
Petrogenesis and geodynamic implications of Ediacaran highly fractionated A-type	858
granitoids in the north Arabian-Nubian Shield (Egypt): constraints from whole-rock	859
geochemistry and Sr-Nd isotopes. <i>Lithos</i> 304–307: 329–346.	860
Samuel, M.D.; Moussa, H.E. and Azer, M.K. 2007. A-type Volcanics in Central Eastern Sinai,	861
Egypt. <i>J. Afr. Earth Sci.</i> 47:203–226.	862
Samuel, M.D.; Moussa, H.E.; Azer, M.K. and Sadek Ghabrial, D.S. 2019. Geochemical	863
constraints of the Ediacaran volcano-sedimentary succession at Wadi Zaghra, Sa'al	864
metamorphic complex, South Sinai, Egypt. <i>Acta Geol. Sin.- Engl.</i> 93: 50–73.	865

Saunders, A.D.; Tarney, J. and Weaver, D. 1980. Transverse geochemical variations across the Antarctic Peninsula: implications for the genesis of Calc-alkaline magmas. *Earth. Planet. Sc. Lett.* 46: 344–360.

Sherif, M.I.; Ghoneim, M.F.; Heikal, M.T.S. and El Dosuky, B.T. 2013. Petrogenesis of granites, Sharm El-Sheikh area, South Sinai, Egypt: petrological constraints and tectonic evolution. *Mineral. Petrol.* 107: 765–783.

Smith, J.V. and Brown, W.L. 1988. *Feldspar Minerals.1 Crystal Structures, Physical, Chemical and Microtextural Properties.* Springer-Verlag, Berlin, Heidelberg, New York, pp. 828

Stein, M. and Goldstein S. 1996. From plume head to continental lithosphere in the Arabian–Nubian Shield. *Nature* 382: 773–778.

Stern, R.J. 1994. Arc assembly and continental collision in the Neoproterozoic East African Orogen: implications for the consolidation of Gondwanaland. *Ann. Rev. Earth Planet. Sci.* 22: 319–351.

Stern, R.J. 2002. Crustal evolution in the East African Orogen: a neodymium isotopic perspective. *J. Afr. Earth. Sci.* 34: 109–117.

Stern, R.J. and Gottfried, D. 1986. Petrogenesis of a Late Precambrian (575-600 Ma) bimodal suite in Northeast Africa. *Contrib. Mineral. Petrol.* 92: 492–501.

Stern, R.J., Voegeli, D.A. 1987. Geochemistry, geochronology, and petrogenesis of a late Precambrian (~590 Ma) composite dike from the North Eastern Desert of Egypt. *Geol. Rundsch.* 76: 325–341.

Stoeser, D.B. 1986 Distribution and tectonic setting of plutonic rocks of the Arabian shield. *J. Afr. Earth Sci.* 4: 21–46.

Stoeser, D.B. and Camp, V.E. 1985. Pan-African microplate accretion of the Arabian Shield.	888
Geol. Soc. Am. Bull. 96: 817–826.	889
Stoeser, D.B. and Elliott, J.E. 1980. Post-orogenic peralkaline and calc-alkaline granites and	890
associated mineralization of the Arabian Shield, Kingdom of Saudi Arabia. Bull. Inst.	891
Applied Geol. King Abdul Aziz Univ. Jeddah 4: 1–23.	892
Stoeser, D.B. and Elliott, J.E. 1984. Plutonic rock distribution map of the northeastern Arabian	893
Shield, Kingdom of Saudi of Saudi Arabia: Saudi Arabian Deputy Ministry for Mineral	894
Resources Open-File Report USGS-OF-04-52, scale 1:500,000. Also, 1985, U.S,	895
Geological Survey Open- File Report 85-264.	896
Stoeser, D.B. and Frost, C.D. 2006. Nd, Pb, Sr, and O isotopic characterization of Saudi Arabian	897
Shield terranes. Chem. Geol. 226: 163–188.	898
Streckeisen, A., 1976. To each plutonic rock its proper name. Earth Sci. Rev. 12: 1–33.	899
Stuckless, J.S.; Hedge, C.E.; Wenner, D.B. and Nkomo, I.T. 1984. Isotopic studies of post-	900
orogenic granites from the northeastern Arabian Shield, Kingdom of Saudi Arabia: Saudi	901
Arabian Deputy Ministry for Mineral Resources Open-File Report USGS-04-42, 40 p.	902
Also, 1985, U.S. Geological Survey Open-File Report 85-726. 57.	903
Sylvester, P.J., 1989. Post-collisional alkaline granites. J. Geol. 97: 261–280.	904
Tollo, R.P.; Aleinikoff, J.N.; Bartholomew, M.J. and Rankin, D.W. 2004. Neoproterozoic A-type	905
granitoids of the central and southern Appalachians: intraplate magmatism associated	906
with episodic rifting of the Rodinian supercontinent. Precambrian. Res. 128: 3–8.	907
Villa, I.G.; Ruggieri, G. and Pux Eoou, M. 1997. Petrological and geochronological	908
discrimination of two white mica generations in a granite cored from the Larderello-	909
Travale geothermal field (Italy). Eur. J. Mineral. 9: 563–568.	910

- Weaver, B.L., 1991. The origin of ocean island basalts end-member compositions: trace elements and isotopic constraints. *Earth Planet. Sc. Lett.* 104: 381–397.
- Wedepohl, K.H. 1994. The composition of the continental crust. *Mineral. Mag.* 58A: 959–960.
- Whalen, J.B.; Currie, K.L. and Chappel, B.W. 1987. A-type granites: geochemical characteristics, discrimination and petrogenesis. *Contrib. Mineral. Petrol.* 95: 407–419.
- Wu, F.-Y.; Sun, D.-y.; Li, H.; Jahn, B.-m. and Wilde, S. 2002. A-type granites in northeastern China: age and geochemical constraints on their petrogenesis. *Chem. Geol.* 187: 143–173.
- Zen, E.A. 1988. Phase relations of peraluminous granitic rocks and their petrogenetic implications. *Ann. Rev. Earth Planet. Sci.* 16: 21–51.
- Zhao, Z.H.; Xiong, X.L.; Han, X.D.; Wang, Y.X.; Wang, Q.; Bao, Z.W. and Jahn, B.M. 2002. Controls on the REE tetrad effect in granites: evidence from the Qianlishan and Baerzhe granites, China. *Geochem. J.* 36: 527–543.

Caption of Figures

Figure 1. General geological map of the Arabian-Nubian shield (After [Johnson and Woldehaimanot, 2003](#)). Basement outcrops are white; Phanerozoic cover is shown in yellow; structural trends are highlighted; ophiolitic rocks are shown in black; and gneissic rocks shown in stipple. The location of the Jabal Aja igneous complex is indicated by a yellow star.

Figure 2. Geological map for Jabal Aja igneous complex (modified after [Hereher and Abdullah., 2017](#)).

- Figure 3.** (a) Granophyre intruded into monzogranite with dykes cutting the monzogranite and abut against the granophyre, (b) peralkaline granite intruded alkali feldspar granite with sharp contact, and (c) Alkali volcanics unconformably overlain on the granophyre.
- Figure 4.** Photomicrographs from different granitic rock of the ARC showing mineralogical and textural variations. (a) Subhedral plagioclase enclosed in coarse perthitic orthoclase, (b) subhedral crystals of biotite, (c) microcline perthite showing cross-hatching twinning, (d) clusters of biotite and muscovite, (e) separate zircon crystal interstitial among feldspar and quartz, (f) anhedral crystals of sodic amphibole, (g) tabular crystal of sodic amphibole altered along the margins into chlorite, (h) discrete crystal of fluorite crystals in interstice between other minerals, (i) anhedral crystals of allanite associated with sodic amphibole, (j) subhedral crystals of primary muscovite associated with sodic amphibole, (k) corroded columbite associated with thorite, and (l) allanite associated with sodic pyroxene.
- Figure 5.** (a) Pyroxene nomenclature based on the classification diagram of Morimoto et al. (1988), (b) TiO_2 -($\text{FeO}_{(t)}+\text{MnO}$)- MgO ternary diagram for classification of biotite (Nachit et al. 2005), (c) $\text{FeO}_{(t)}$ vs. Al_2O_3 discrimination diagram for biotite (Abdel-Rahman 1994), (d) Mg vs. Al diagram of biotite (after Nachit et al., 1985), (e) compositional fields for primary and secondary muscovite (Miller et al., 1981); Ti, Mg, and Na = apfu, and (f) classification of the analyzed amphiboles (after Leake, 1997).
- Figure 6.** Classification of the granites of the ARC intrusion using the R_1 - R_2 diagram of De la Roche et al. (1980).
- Figure 7.** Variation diagrams of major oxide against SiO_2 .
- Figure 8.** Variation diagrams of certain trace elements against SiO_2 .

Figure 9. (a) Mid-ocean ridge basalt (MORB)-normalized trace element diagram for the averages of the ARC granites, (b) chondrite-normalized rare-earth element patterns for the averages of the ARC granites, (c) mid-ocean ridge basalt (MORB)-normalized trace element diagram for MMEs, and (d) chondrite-normalized rare-earth element patterns for MMEs. Normalization values in (a, c) from [Pearce \(1983\)](#) and in (b, d) from [Evensen et al. \(1978\)](#).

Figure 10. (a) $\text{Al}_2\text{O}_3/(\text{Na}_2\text{O}+\text{K}_2\text{O})$ vs. $\text{Al}_2\text{O}_3/(\text{CaO}+\text{Na}_2\text{O}+\text{K}_2\text{O}_3)$ diagram for the granitic rocks of the ARC (after [Maniar and Piccoli, 1989](#)), (b) discrimination diagram of [Sylvester \(1989\)](#) for rocks with > 68 wt.% SiO_2 , (c) Ga/Al vs. $\text{FeO}_{\text{(t)}}/\text{MgO}$ diagram of [Whalen et al. \(1987\)](#), (d) $\text{Y}+\text{Nb}$ vs. Rb tectonic discrimination diagram of [Pearce et al. \(1984\)](#), (e) $\text{Hf}-\text{Rb}/30-3*\text{Ta}$ ternary diagram (after [Harris et al., 1986](#)), and (f) plots of ARC granites on the tectonic discrimination (R_1-R_2) of [Batchelor and Bowden \(1985\)](#).

Figure 11. (a) Y/Nb vs. Rb/Nb (after [Eby 1990](#)); symbols as in Figure 6; A1=A-type granitoids with an OIB-type source, A2= A-type granitoids with crustal derived magma, and (b) simplified sketch for the tectonomagmatic evolution of the A-type granites of the ARC, showing partial melting of the lower crust due to an upwelling of asthenosphere mantle material as a result of lithospheric delamination.

Figure 12. (a) Sr vs. Ba , (b) Sr vs. Rb/Sr , and (c) Rb vs. K/Rb for the granitic rocks of the ARC.

Cover letter

To: Journal of Geology

Dear Editor (Dear Prof. David B Rowley)

The Attached files concern the my accepted manuscript (MS. No. **80910**) which was accepted with minor revisions. The old title of my manuscript is “*Petrological and Geochemical Evolution of Ediacaran Rare-metal-bearing Aja Ring Complex A-type Granites, Northern Arabian Shield, Saudi Arabia*”, but I modified the title into “*Genesis and Petrology of Post-collisional Rare metal-bearing Granites in the Arabian Shield: A case study of Aja Ring Complex, Northern Saudi Arabia*”

I accepted and performed all the corrections suggested by the reviewer and editor. The detail responses to the reviewer and the editor are listed in as separated file (Revisions and Response Letter), while the other minor comments including corrections are performed in the revised manuscript. Also, each point of the reviewers' comments has been incorporated and indicated in the "Marked Version" of the manuscript using "Track Changes". I submitted both a “Clean Version” and a "Marked Version" of the manuscript using "Track Changes".

The revised manuscript includes the revised text, figures and tables. The microprobe tables (Table 1S-9S) will publish as online supplements.

Corresponding Author

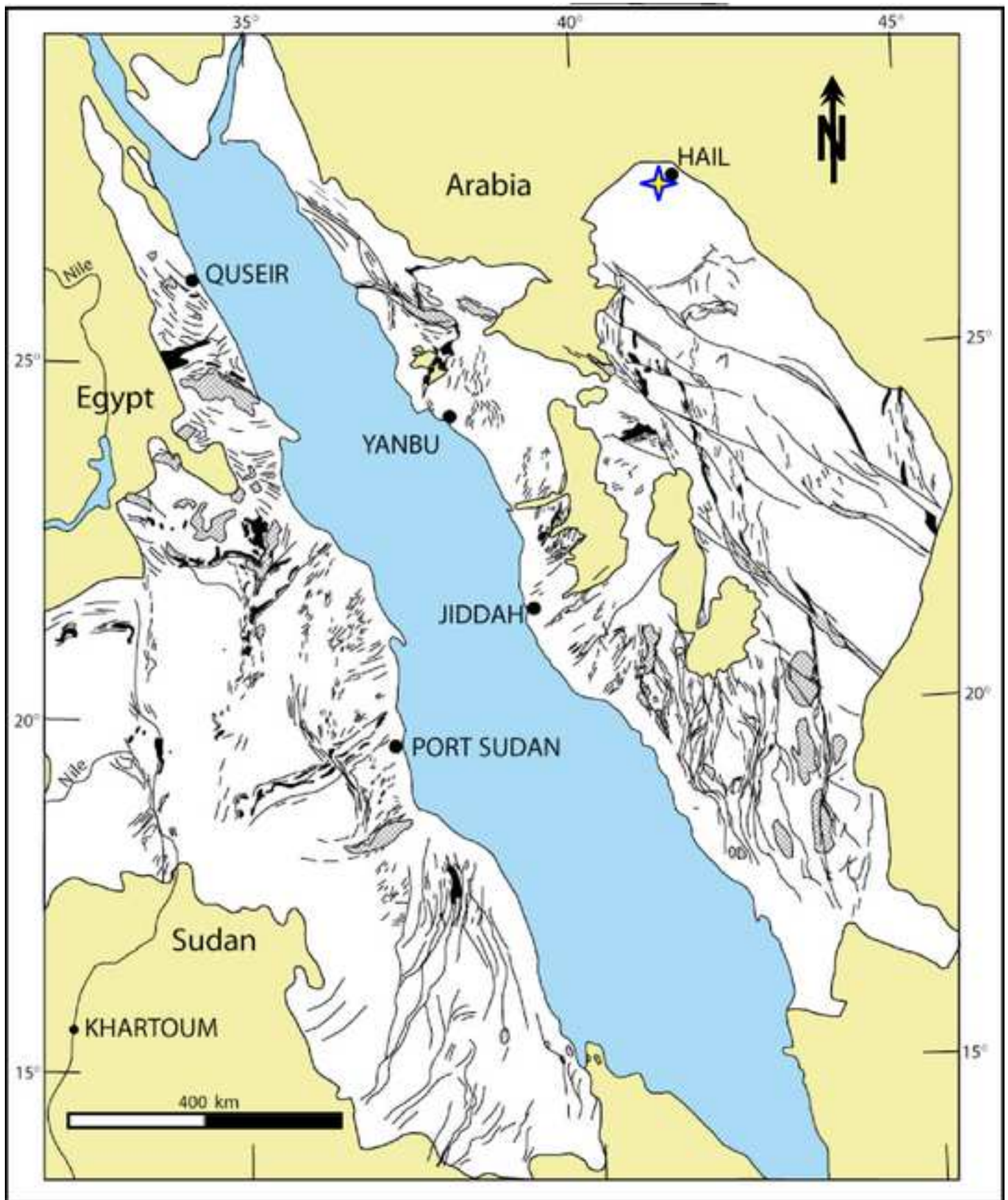
Dr. Bassam A. Abuamarah

Professor of Igneous and Metamorphic Petrology

Department of Geology and Geophysics, College of Science,

King Saud University

Saudi Arabia.

**Figure 1**

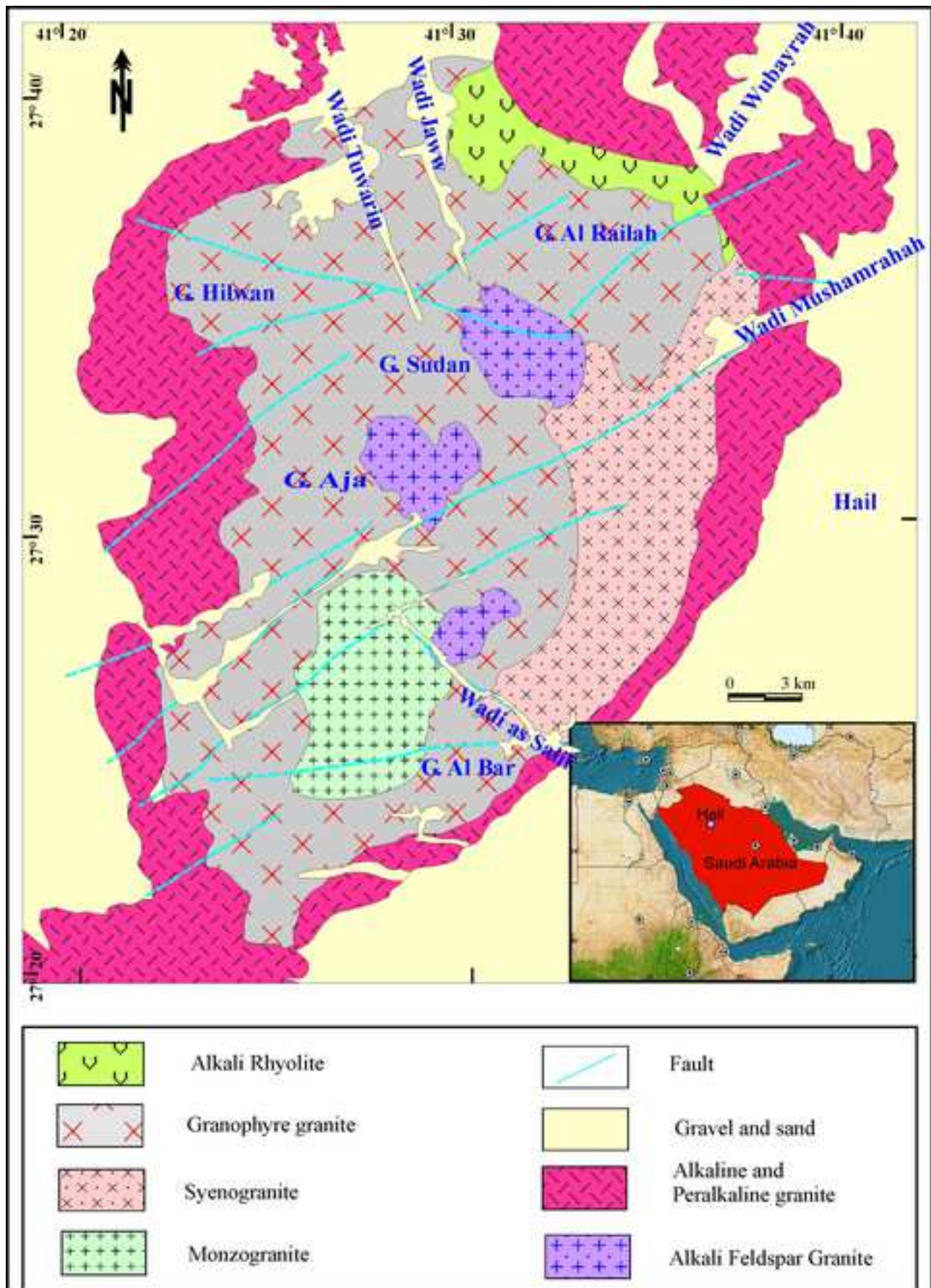


Figure 2

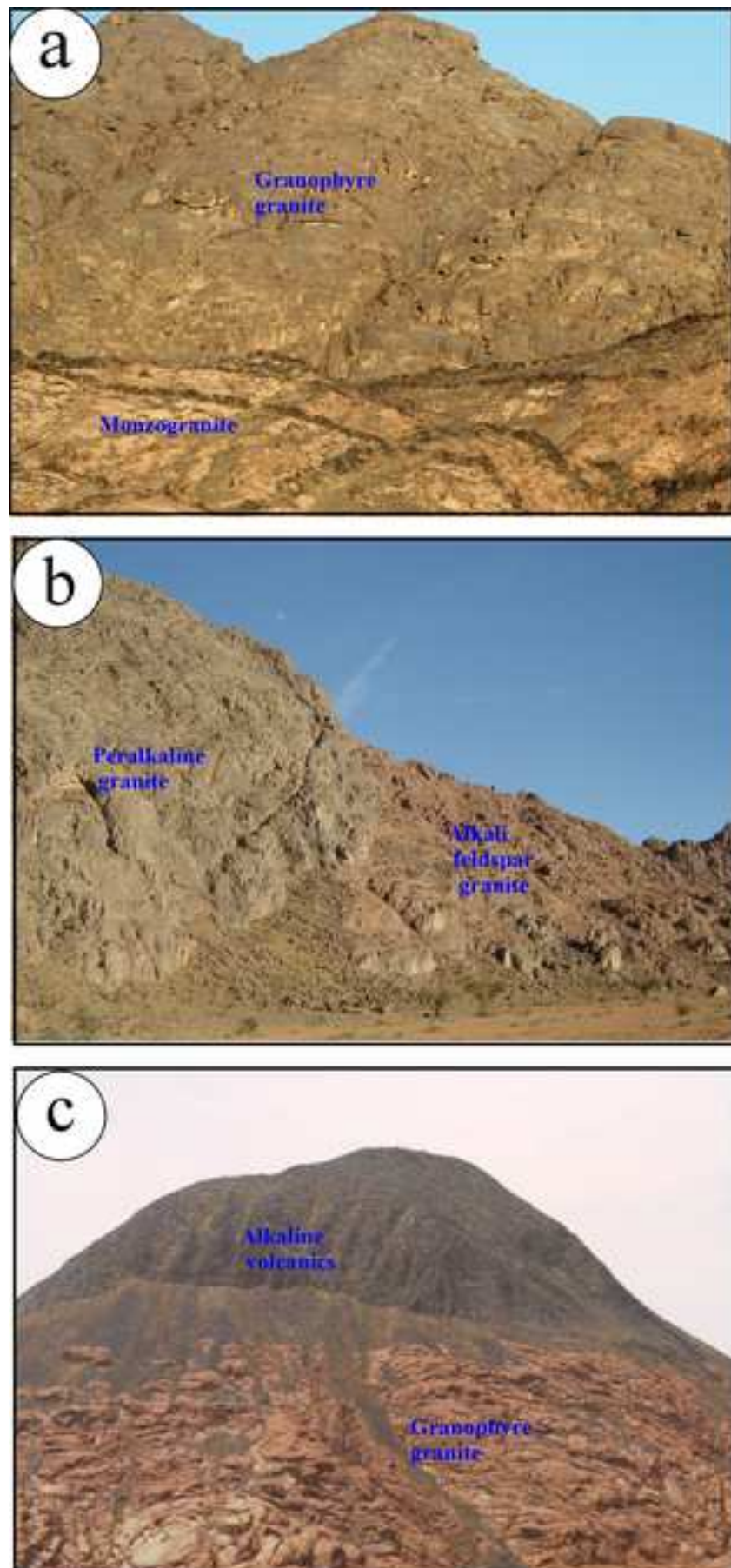


Figure 3

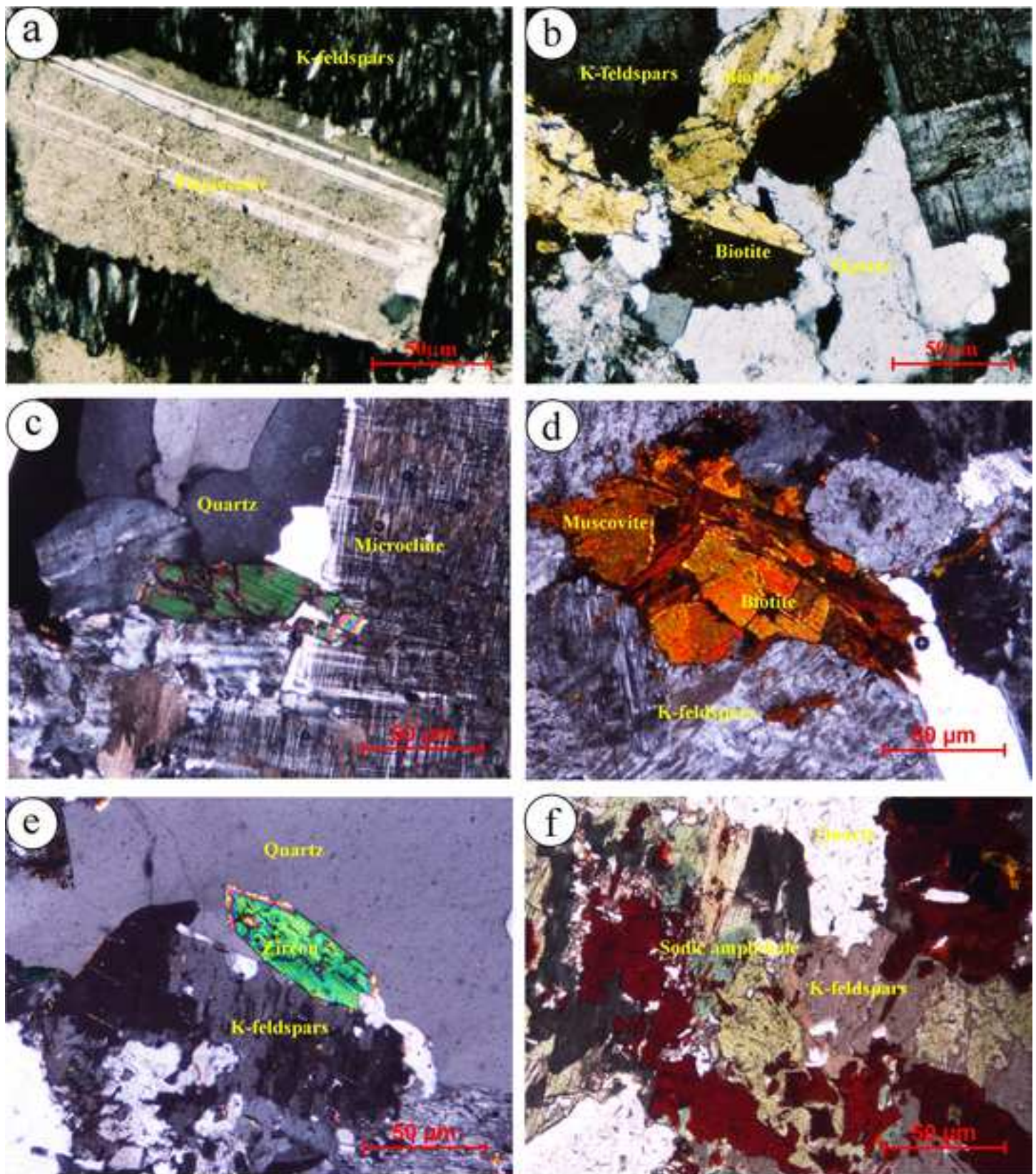


Figure 4

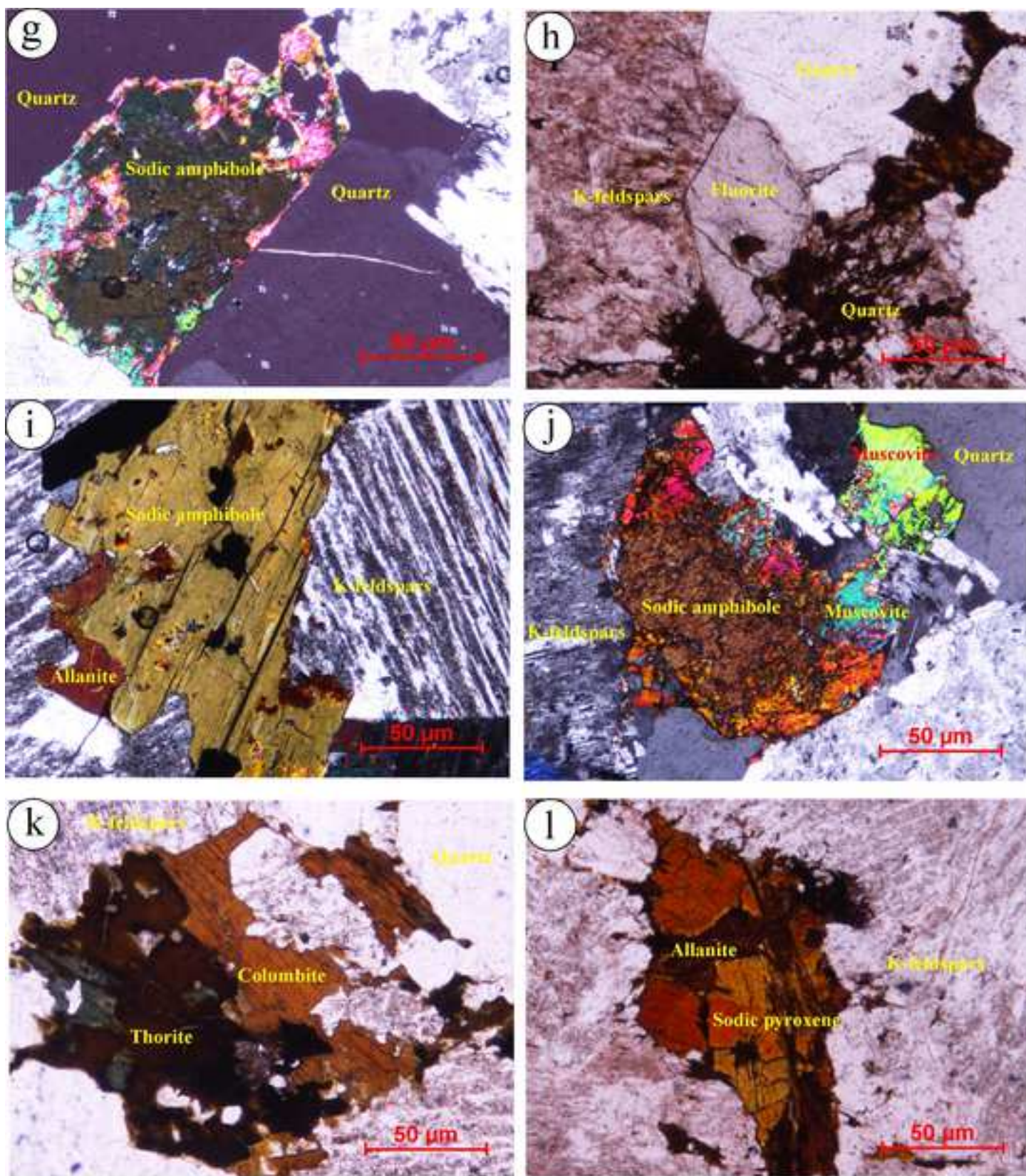


Figure 4 cont.

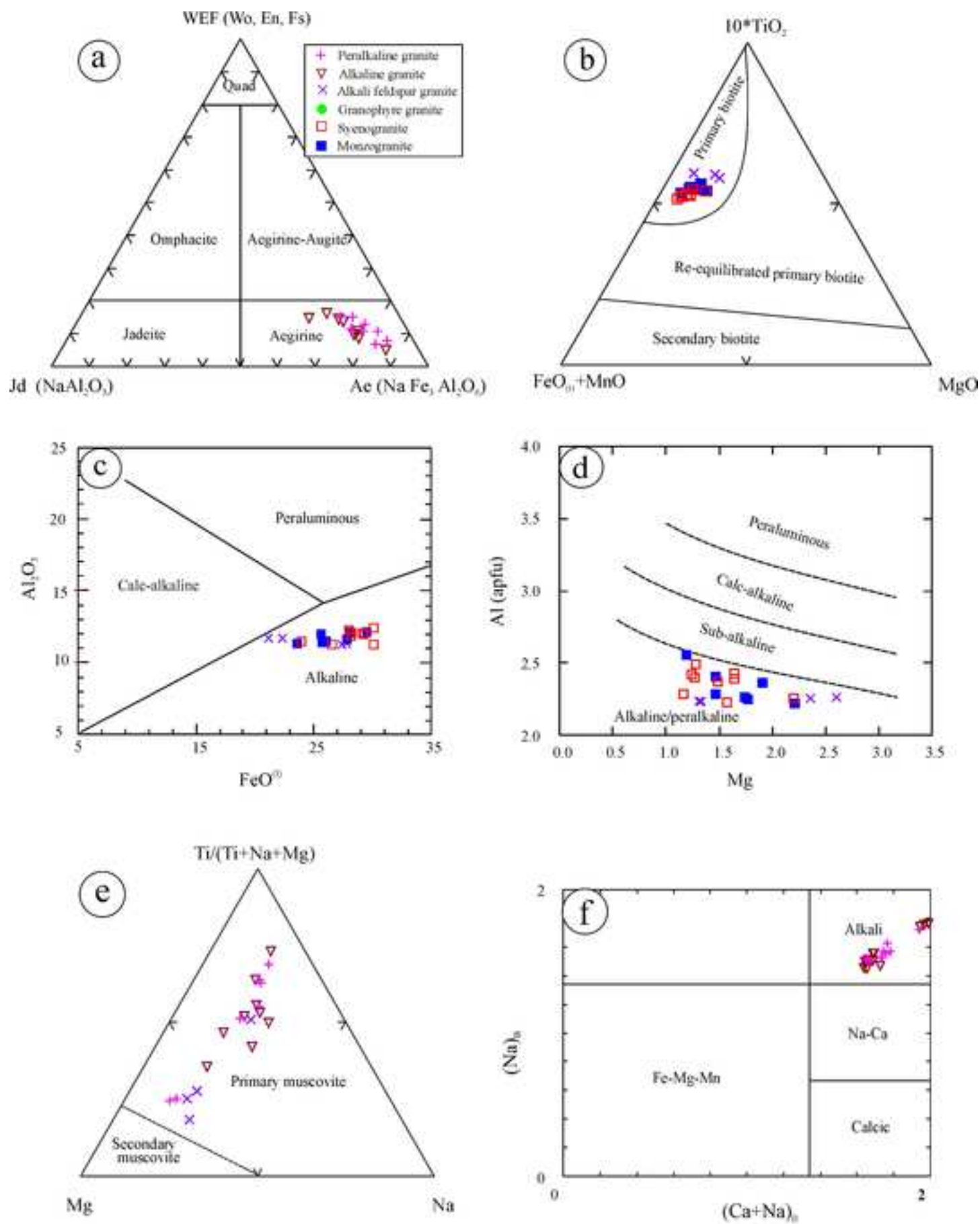


Figure 5

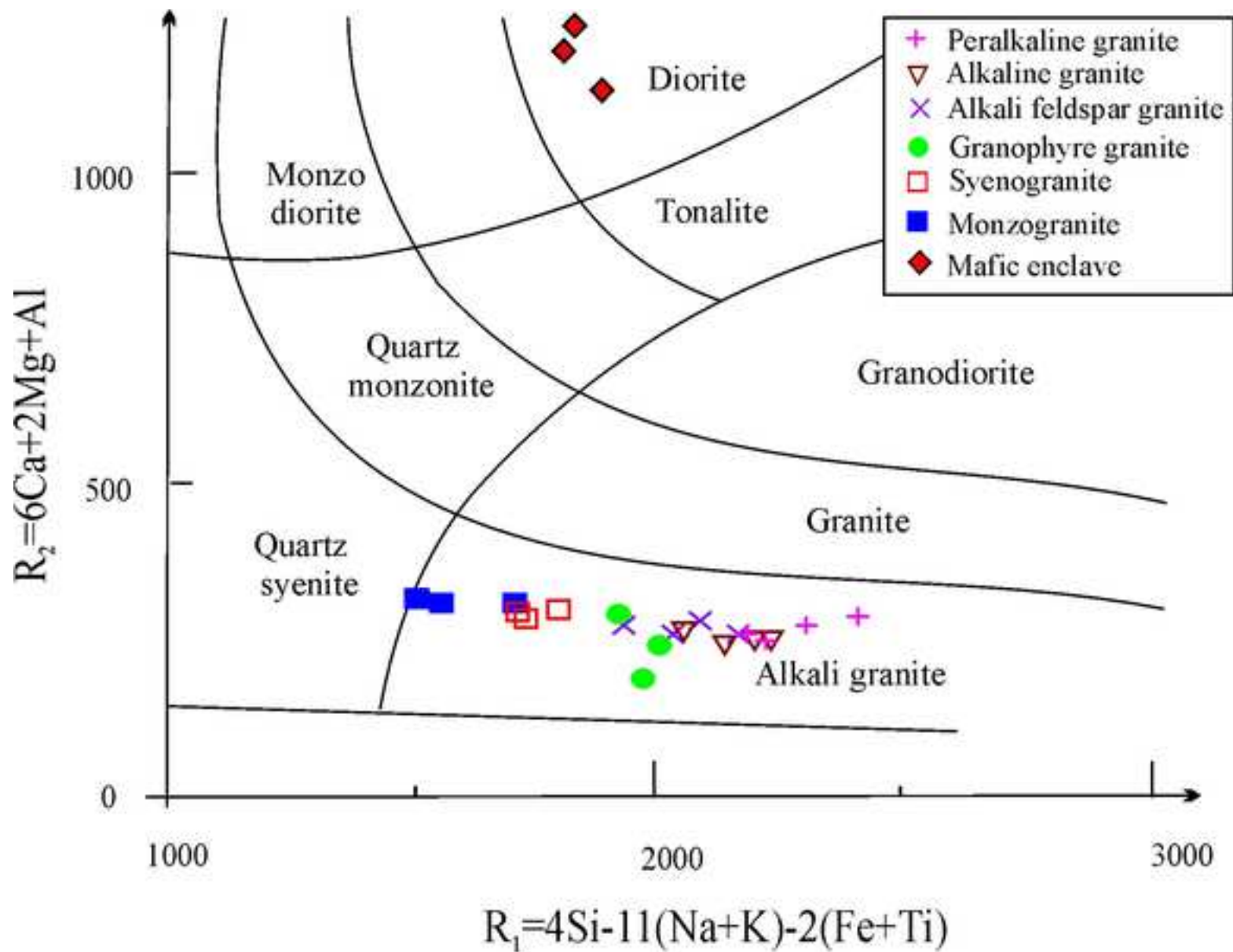


Figure 6

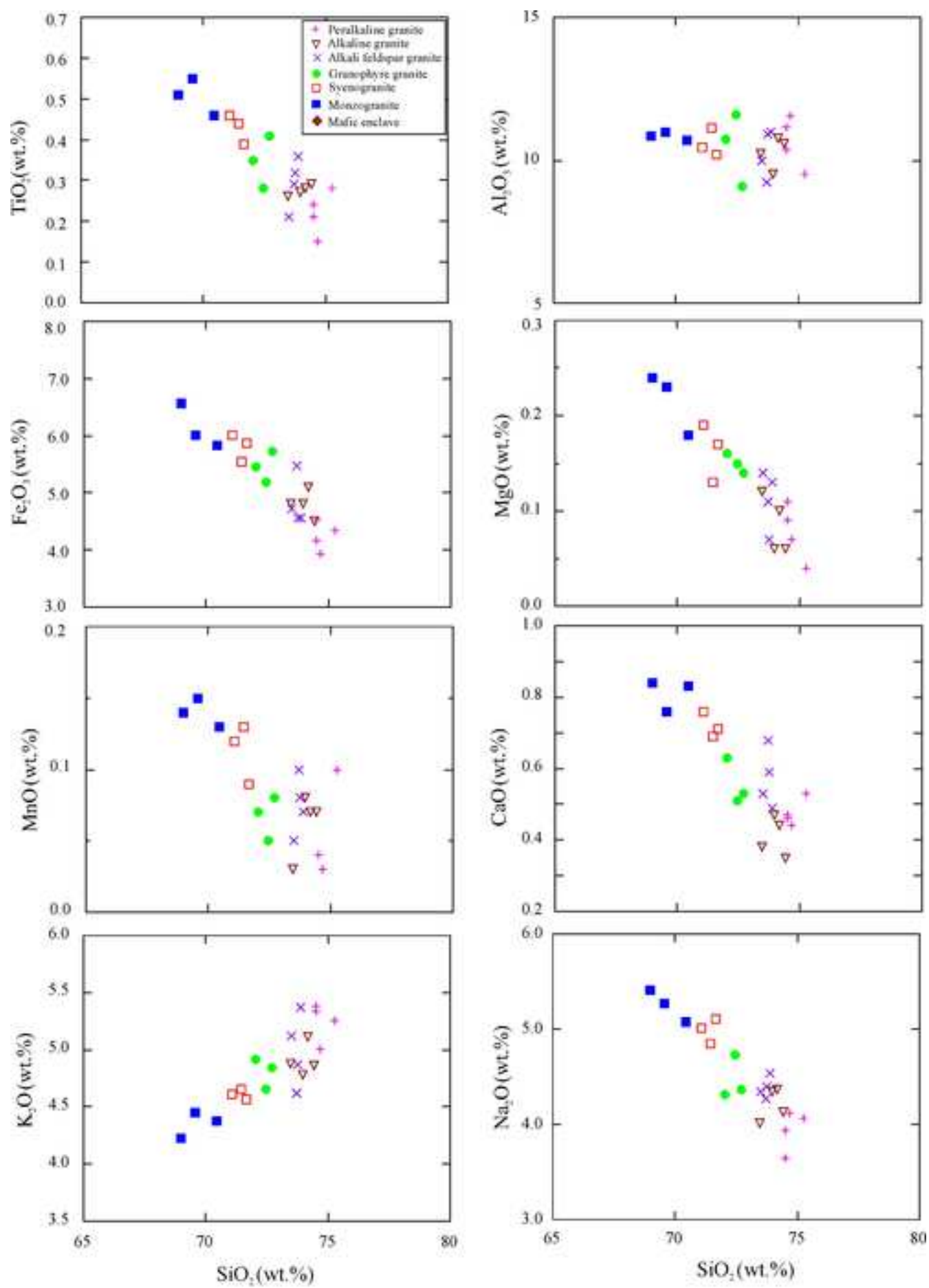


Figure 7

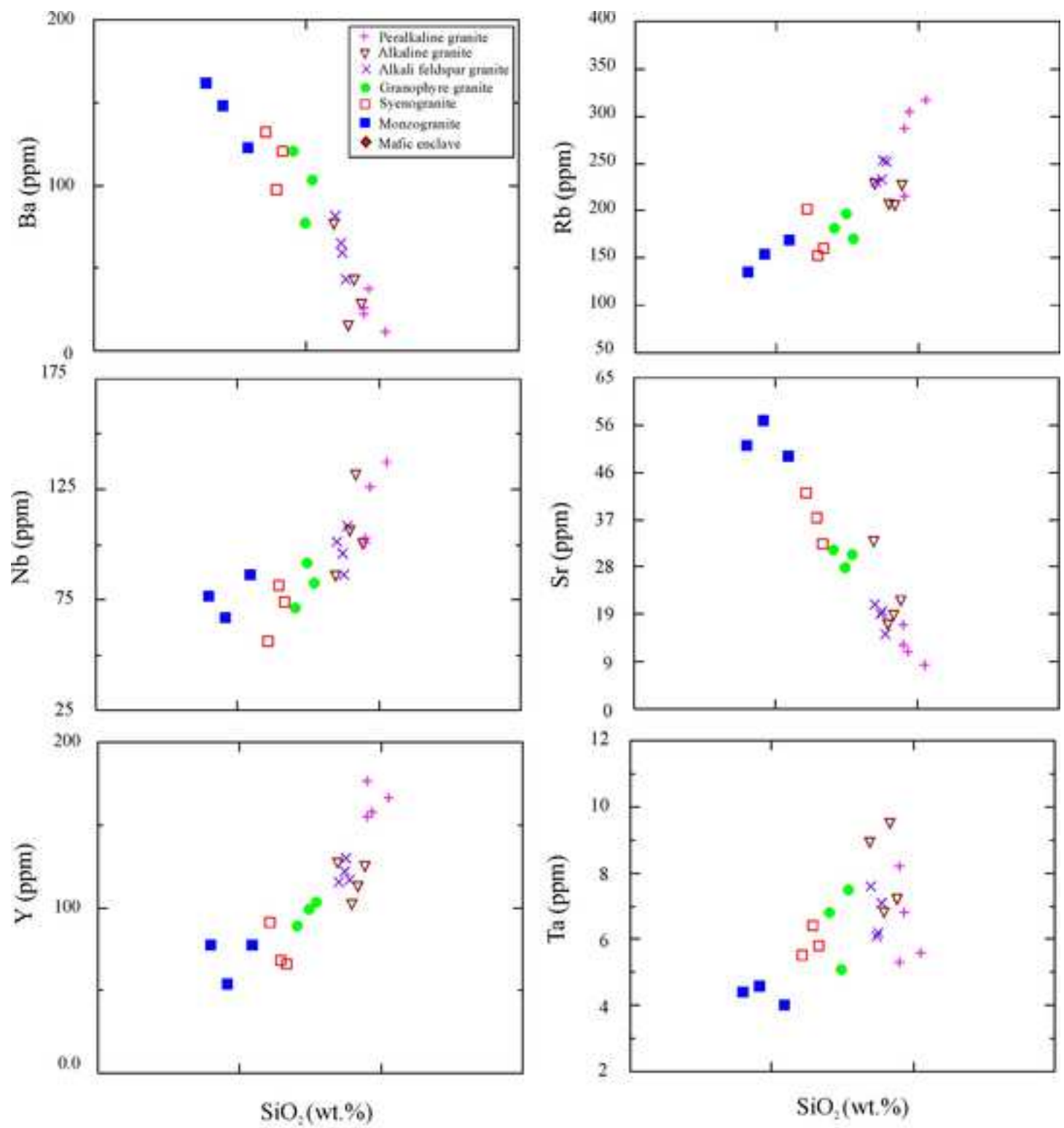


Figure 8

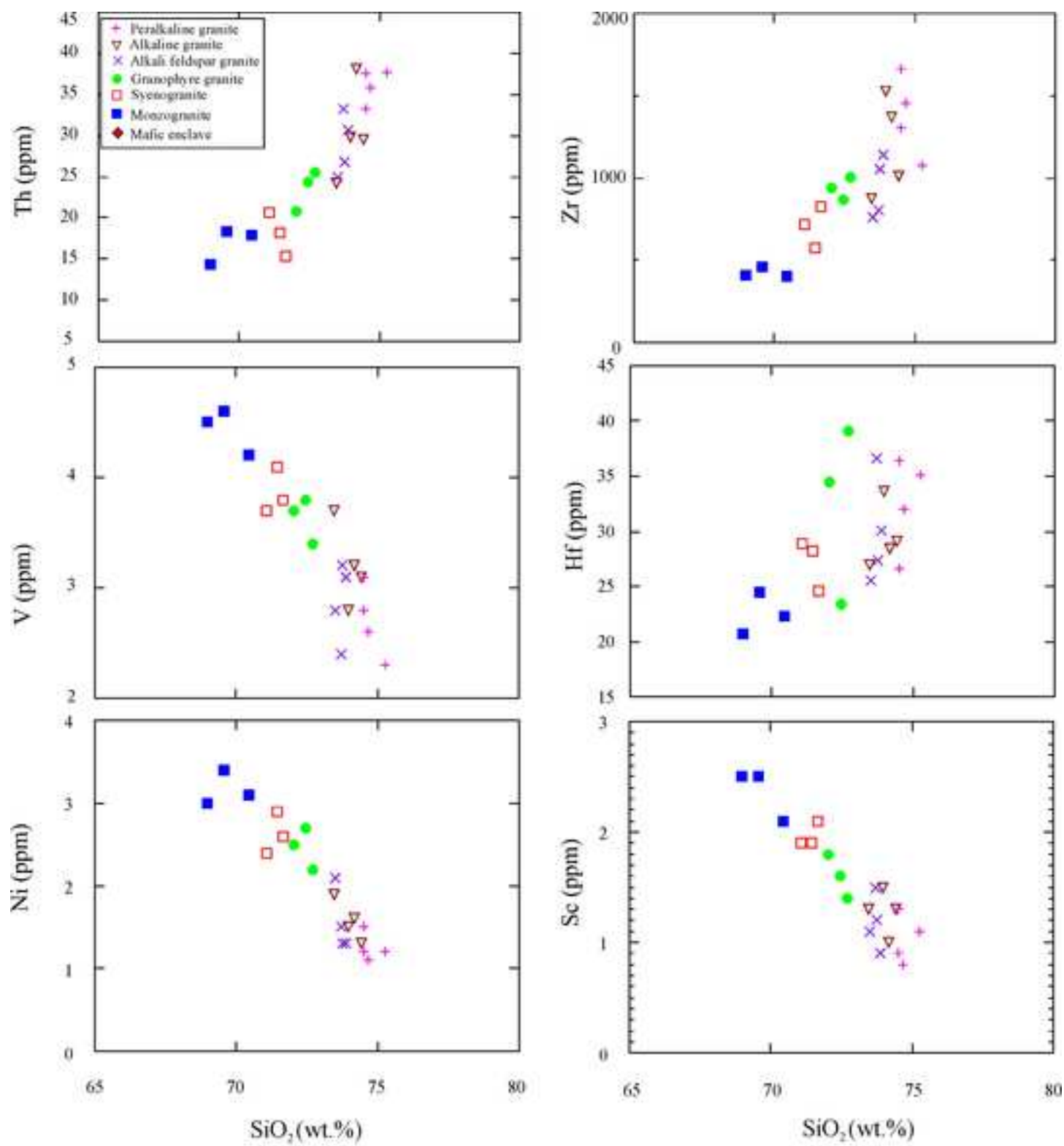


Figure 8 Cont.

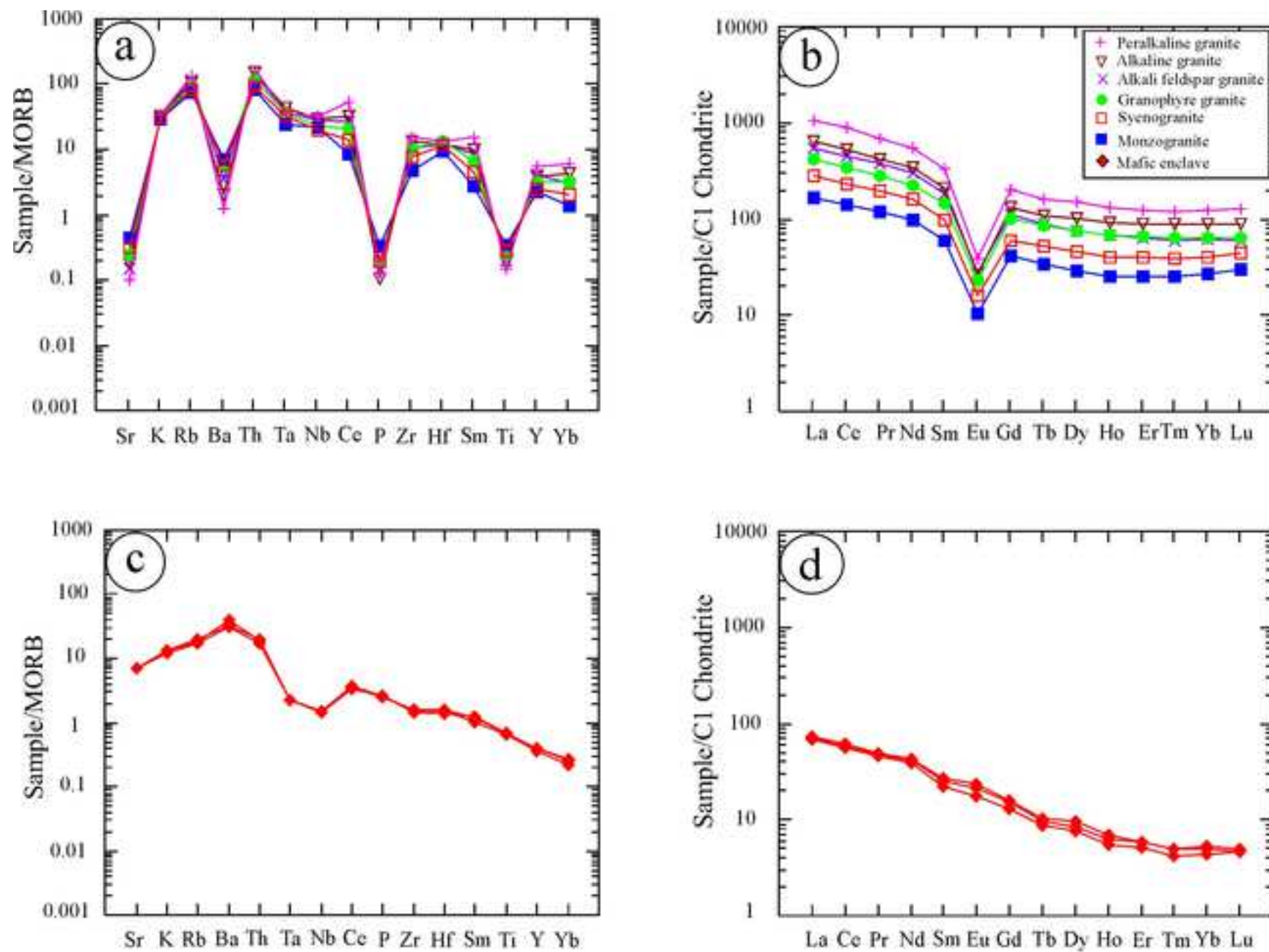


Figure 9

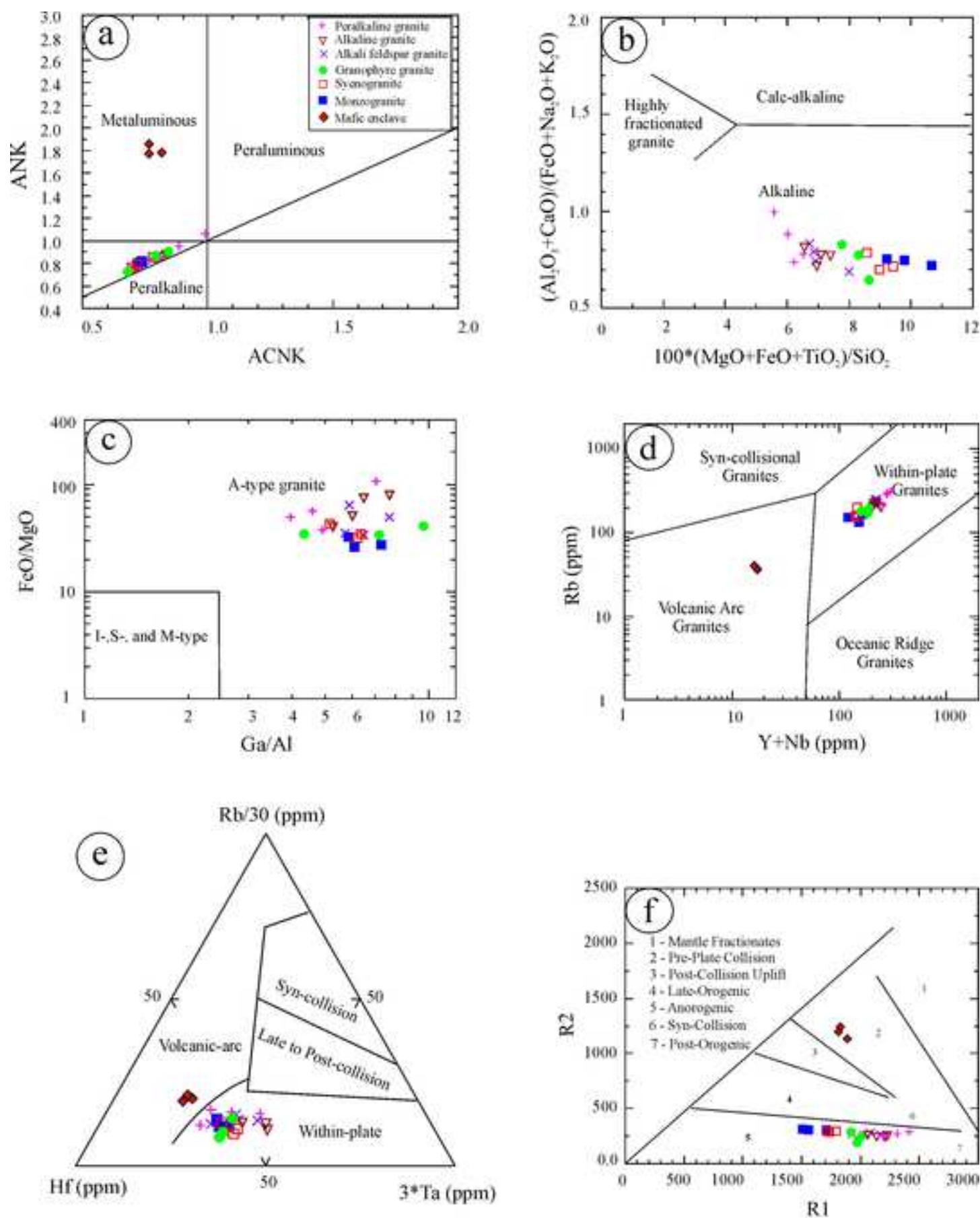


Figure 10

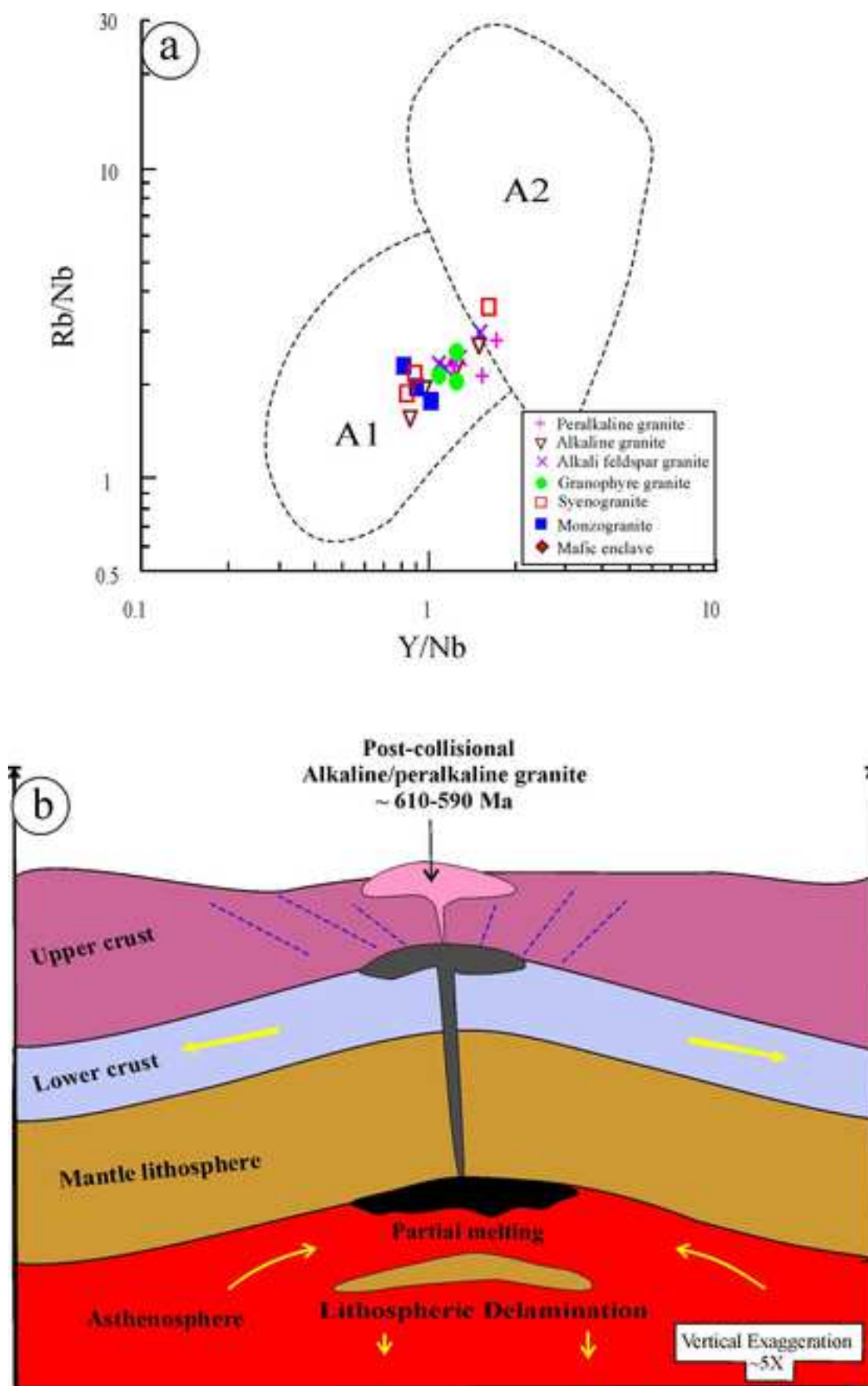


Figure 11

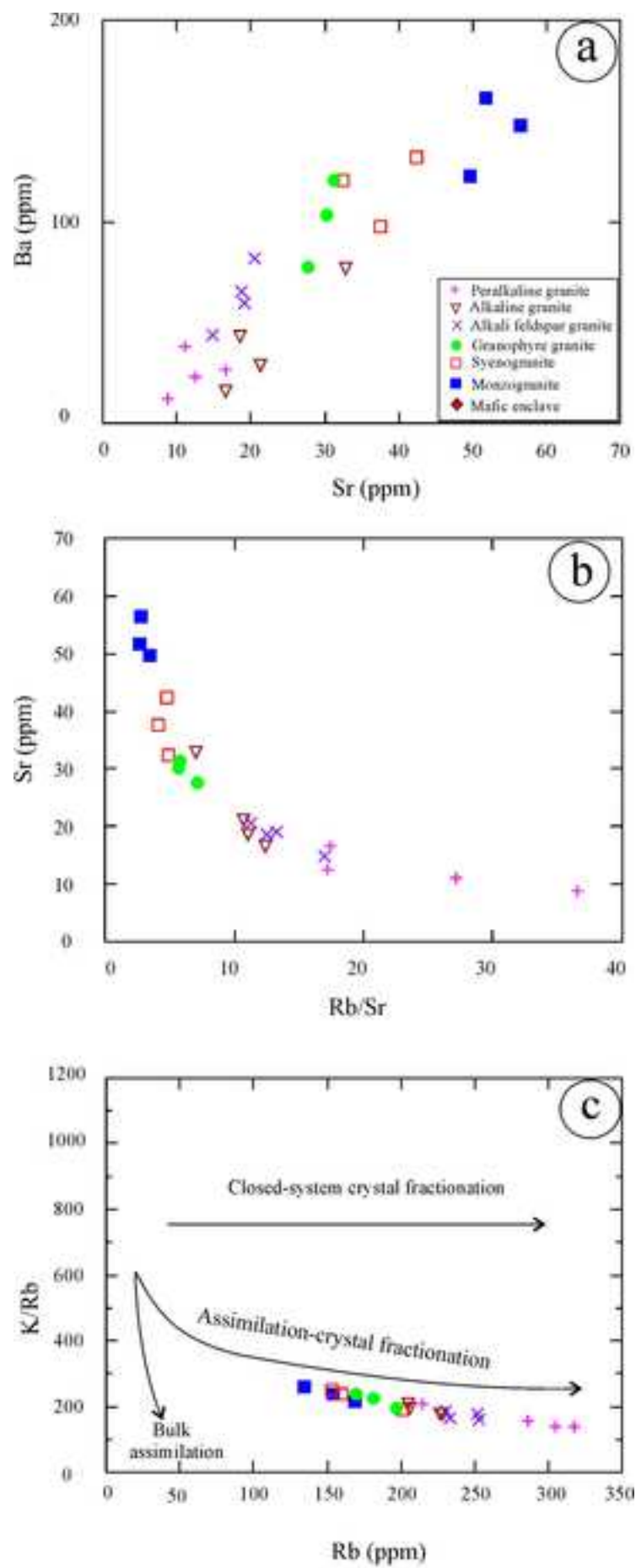


Figure 12

Table-1

Table 1 : Major oxide and trace element contents of Aja ring complex granites and mafic microgranular enclaves

Rock type	Monzogranite				Syenogranite				Granophyre				Alkali feldspar granite				
Sample	AJ-1	AJ-2	AJ-3	Av.	AJ-4	AJ-5	AJ-6	Av.	AJ-7	AJ-8	AJ-9	Av.	AJ-11	AJ-12	AJ-13	AJ-14	Av.
SiO ₂	69.56	68.97	70.44	69.66	71.45	71.67	71.06	71.39	72.47	72.05	72.69	72.40	73.52	73.73	73.75	73.9	73.73
TiO ₂	0.55	0.51	0.46	0.51	0.44	0.39	0.46	0.43	0.28	0.35	0.41	0.35	0.21	0.29	0.32	0.36	0.30
Al ₂ O ₃	10.99	10.84	10.69	10.84	11.12	10.19	10.45	10.59	11.58	10.73	9.08	10.46	9.99	9.22	10.93	10.98	10.28
Fe ₂ O ₃	6.01	6.57	5.84	6.14	5.54	5.86	6.02	5.81	5.18	5.46	5.72	5.45	4.72	5.47	4.56	4.56	4.83
MnO	0.15	0.14	0.13	0.14	0.13	0.09	0.12	0.11	0.05	0.07	0.08	0.07	0.05	0.1	0.08	0.07	0.08
MgO	0.23	0.24	0.18	0.22	0.13	0.17	0.19	0.16	0.15	0.16	0.14	0.15	0.14	0.11	0.07	0.13	0.11
CaO	0.76	0.84	0.83	0.81	0.69	0.71	0.76	0.72	0.51	0.63	0.53	0.56	0.53	0.68	0.59	0.49	0.57
Na ₂ O	5.27	5.41	5.07	5.25	4.85	5.11	5.01	4.99	4.73	4.31	4.37	4.47	4.35	4.27	4.4	4.54	4.39
K ₂ O	4.45	4.23	4.38	4.35	4.66	4.57	4.61	4.61	4.66	4.92	4.84	4.81	5.12	4.62	4.87	5.37	5.00
P ₂ O ₅	0.05	0.03	0.04	0.04	0.03	0.02	0.02	0.02	0.03	0.02	0.02	0.02	0.01	0.01	0.02	0.03	0.02
LOI	1	1.38	0.72	1.03	0.95	0.65	1.05	0.88	0.85	0.85	1.14	0.95	0.91	0.52	0.25	0.19	0.47
Total	99.02	99.16	98.78	98.99	99.99	99.43	99.75	99.72	100.49	99.55	99.02	99.69	99.55	99.02	99.84	100.62	99.76
Cs	4.5	2.1	1.8	2.80	1.6	1.1	1	1.23	1.9	1.3	1.8	1.67	1	1.3	1.4	0.8	1.13
Ba	147.3	161.4	122.4	143.70	97.4	120.8	132.1	116.77	123.6	120.7	103.4	115.90	81.6	65.2	99.4	43.5	72.43
Rb	154.6	135.2	168.7	152.83	153.5	160.3	201.5	171.77	197.2	181.8	170.5	183.17	231.2	233.6	253	251.8	242.40
Sr	56.5	51.8	49.7	52.67	37.6	32.5	42.4	37.50	27.7	31.3	30.2	29.73	20.6	18.7	19.1	14.8	18.30
Nb	67	76.4	86.4	76.60	81.7	74.1	56.4	70.73	91.5	71.4	82.7	81.87	101.4	96.2	86.2	108.4	98.05
Ta	4.6	4.4	4	4.33	6.4	5.8	5.5	5.90	5.1	6.8	7.5	6.47	7.6	6.1	6.2	7.1	6.75
Y	54.2	77.2	77.4	69.60	68.2	66.1	90.8	75.03	99.1	88.9	103.4	97.13	115.5	122	129.8	117.2	121.13
Ga	35.6	42.1	33.2	36.97	30.5	34.3	34.5	33.10	26.6	41	47.2	38.27	34.4	37.9	34.2	33.4	34.98
Th	18.3	14.3	17.9	16.83	18.2	15.4	20.7	18.10	24.3	20.8	25.5	23.53	25	33.3	26.8	30.6	28.93
Zr	456.4	409.8	403.6	423.27	573.3	827.2	717.2	705.90	871.2	937.2	1006.6	938.33	763.4	806.5	1052.6	1141.2	940.93
Hf	24.5	20.7	22.3	22.50	28.2	24.6	28.9	27.23	23.4	34.5	39.1	32.33	25.6	36.6	27.4	30.1	29.93
Ni	3.4	3	3.1	3.17	2.9	2.6	2.4	2.63	2.7	2.5	2.2	2.47	2.1	1.5	1.3	1.3	1.55
Co	8.4	7.9	7.6	7.97	8.6	9.3	2.7	6.87	5.1	4	3.5	4.20	3.7	3.8	3.1	3.4	3.50
Sc	2.5	2.5	2.1	2.37	1.9	2.1	1.9	1.97	1.6	1.8	1.4	1.60	1.1	1.5	1.2	0.9	1.18
V	4.6	4.5	4.2	4.43	4.1	3.8	3.7	3.87	3.8	3.7	3.4	3.63	2.8	2.4	3.2	3.1	2.88
Cu	15.2	18.8	16.7	16.90	12.6	14.4	18.3	15.10	14.4	16.4	19.2	16.67	11.4	4.4	3.8	5.3	6.23
Pb	49.8	22.3	28.8	33.63	21.7	27.3	25.2	24.73	17.5	16.8	47.5	27.27	23.4	43.7	18.9	20.7	26.68
Zn	99.7	476.8	69.4	215.30	78.7	69.6	148.1	98.80	60.5	149.4	255.8	155.23	147.6	432.5	197.7	188.3	241.53
U	14.7	10.1	8.5	11.10	7.3	6.4	7.8	7.17	7.8	8.6	12.7	9.70	8.4	11.2	4.6	3.8	7.00
Mg#	7.05	6.75	5.75	6.52	4.44	5.43	5.88	5.25	5.43	5.49	4.62	5.18	5.55	3.83	2.95	5.35	4.42
ASI	0.74	0.72	0.73	0.73	0.78	0.70	0.71	0.73	0.84	0.79	0.68	0.77	0.73	0.69	0.80	0.77	0.75
AI	1.23	1.24	1.22	1.23	1.17	1.31	1.27	1.25	1.11	1.16	1.37	1.21	1.27	1.31	1.15	1.21	1.23

Table 1. Cont.

Rock type	Alkaline granite					Peralakine granite					Mafic enclaves			
Sample	AJ-10	AJ-15	AJ-16	AJ-17	Av.	AJ-18	AJ-19	AJ-20	AJ-21	Av.	MME-3	MME-5	MME-8	Av.
SiO2	73.46	73.98	74.17	74.42	74.01	74.49	74.53	74.69	75.27	74.75	57.16	57.85	58.54	57.85
TiO2	0.26	0.27	0.28	0.29	0.28	0.24	0.21	0.15	0.28	0.22	1.04	1.02	0.99	1.02
Al2O3	10.23	9.52	10.77	10.59	10.28	10.36	11.16	11.57	9.53	10.66	15.27	15.1	15.06	15.14
Fe2O3	4.82	4.81	5.09	4.51	4.81	4.52	4.16	3.94	4.34	4.24	7.01	6.86	6.61	6.83
MnO	0.03	0.08	0.07	0.07	0.06	0.04	0.04	0.03	0.1	0.05	0.11	0.1	0.09	0.10
MgO	0.12	0.06	0.1	0.06	0.09	0.09	0.11	0.07	0.04	0.08	4.99	4.9	5.02	4.97
CaO	0.38	0.47	0.44	0.35	0.41	0.47	0.46	0.44	0.53	0.48	6.46	6.13	5.49	6.03
Na2O	4.01	4.34	4.37	4.13	4.21	3.94	3.65	4.12	4.07	3.95	3.77	3.85	3.77	3.80
K2O	4.88	4.78	5.11	4.86	4.91	5.38	5.34	5.01	5.26	5.25	1.83	2.01	2.04	1.96
P2O5	0.02	0.01	0.01	0.01	0.01	0.02	0.01	0.02	0.01	0.02	0.31	0.3	0.32	0.31
LOI	0.96	0.79	0.5	0.28	0.63	0.76	0.55	1.17	0.4	0.72	1.61	1.49	1.72	1.61
Total	99.17	99.11	100.91	99.57	99.69	100.31	100.22	101.21	99.83	100.39	99.56	99.61	99.65	99.61
Cs	1.4	1.4	1.5	1.3	1.40	1.1	2	1.5	1	1.40	2.4	1.9	2.2	2.17
Ba	76.6	16.2	43	28.5	41.08	23.1	26.5	38.4	12.6	25.15	635.3	788.6	655.9	693.27
Rb	228.6	206.4	205.1	226.6	216.68	215.1	286.6	304.6	317.7	281.00	35.1	36.7	39.4	37.07
Sr	32.8	16.6	18.5	21.2	22.28	12.5	16.5	11.2	8.7	12.23	837.3	858.6	866.7	854.20
Nb	85.6	106.2	131.6	100.5	105.98	100.8	103.1	126.1	137.4	116.85	5.3	5.3	5.2	5.27
Ta	8.9	6.8	9.5	7.2	8.10	5.3	8.2	6.8	5.6	6.48	0.4	0.4	0.4	0.40
Y	127	101.6	112.8	124.5	116.48	154.6	176.1	157.5	166.3	163.63	12	11.9	10.9	11.60
Ga	28.7	39	34.5	36.4	34.65	21.8	29.2	29.4	35.8	29.05	16	15.7	16.5	16.07
Th	24.2	29.8	38.1	29.5	30.40	33.2	37.5	35.8	37.7	36.05	3.5	3.8	3.9	3.73
Zr	875.3	1528.5	1372	1013.4	1197.30	1305	1660.1	1458.3	1076.2	1374.90	132.7	146.2	137.4	138.77
Hf	26.9	33.6	28.5	29.1	29.53	36.4	26.6	32	35.1	32.53	3.4	3.9	3.7	3.67
Ni	1.9	1.5	1.6	1.3	1.58	1.2	1.5	1.1	1.2	1.25	94.8	85.1	104.5	94.80
Co	4.2	3.7	4	3.7	3.90	4.5	3.4	3.2	3.1	3.55	26.2	23	25.7	24.97
Sc	1.3	1.5	1	1.3	1.28	1.3	0.9	0.8	1.1	1.03	15.2	14.2	13.3	14.23
V	3.7	2.8	3.2	3.1	3.20	3.1	2.8	2.6	2.3	2.70	130.1	123.9	125.8	126.60
Cu	10.1	4.4	6.4	5.2	6.53	9.5	8.2	7.3	3.8	7.20	25.2	43.7	41.8	36.90
Pb	22.4	31.2	22.8	25.4	25.45	16.4	17.2	16.7	87.6	34.48	6.2	5.9	6.9	6.33
Zn	144.1	379.7	64.7	261.8	212.58	63.7	89.1	91.4	281.7	131.48	52.9	46.5	57.1	52.17
U	9.2	7.7	12.1	5.7	8.68	7.7	12.3	10.1	8.3	9.60	1.4	1.4	1.69	1.50
Mg#	4.70	2.41	3.75	2.57	3.36	3.80	4.98	3.40	1.79	3.49	58.51	58.59	60.07	59.06
ASI	0.81	0.72	0.80	0.83	0.79	0.79	0.88	0.89	0.71	0.82	0.77	0.77	0.82	0.78
AI	1.16	1.29	1.18	1.14	1.19	1.19	1.06	1.06	1.30	1.15	0.54	0.56	0.56	0.55

Table 2. Normative mineral compositions for the Aja ring complex granites and mafic microgranular enclaves.

Rock type	Monzogranite				Syenogranite				Granophyre				Alkali feldspar granite				
Sample No.	AJ-1	AJ-2	AJ-3	Av.	AJ-4	AJ-5	AJ-6	Av.	AJ-7	AJ-8	AJ-9	Av.	AJ-11	AJ-12	AJ-13	AJ-14	Av.
Quartz	24.14	23.44	26.26	24.61	26.21	28.74	27.25	27.40	26.24	28.51	34.35	29.70	32.71	34.98	30.17	29.54	31.85
Orthoclase	26.96	25.71	26.53	26.40	27.93	27.48	27.74	27.72	27.76	29.59	29.36	28.90	30.8	27.85	29.01	31.72	29.85
Albite	32.54	33.1	31.34	32.33	31.68	27.42	28.58	29.23	33.86	28.27	20.27	27.47	23.27	22.12	29.32	26.54	25.31
Anorthite	-	-	-	-	-	-	-	-	-	-	-	-	-	-	-	-	-
Acmite	2.99	3.23	2.87	3.03	2.7	2.8	2.92	2.81	2.41	2.6	2.77	2.59	2.2	2.6	2.17	2.17	2.29
Na-Metasilicate	2.28	2.4	2.18	2.29	1.6	3.12	2.62	2.45	0.87	1.37	3.39	1.88	2.72	2.74	1.34	2.19	2.25
Diopside	3.11	3.6	3.49	3.40	2.9	3.05	3.27	3.07	2.08	2.69	2.27	2.35	2.31	2.99	2.5	1.97	2.44
Hypersthene	6.77	7.44	6.34	6.85	6.05	6.58	6.67	6.43	6.16	6.23	6.74	6.38	5.56	6.13	4.82	5.11	5.41
Magnetite	-	-	-	-	-	-	-	-	-	-	-	-	-	-	-	-	-
Ilmenite	1.07	1	0.9	0.99	0.85	0.75	0.89	0.83	0.54	0.68	0.8	0.67	0.41	0.56	0.61	0.68	0.57
Apatite	0.11	0.07	0.09	0.09	0.07	0.04	0.04	0.05	0.07	0.04	0.04	0.05	0.02	0.02	0.04	0.07	0.04
Colour Index	10.96	12.03	10.72	11.24	9.79	10.39	10.83	10.34	8.77	9.6	9.81	9.39	8.27	9.68	7.93	7.77	8.41
Diff. Index	84	82	84	83.34	86	84	84	84.34	88	86	84	86.07	87	85	89	88	87.00

Table 2. Cont

Rock type	Alkaline granite					Peralkaline granite					Mafic enclaves			
Sample No.	AJ-10	AJ-15	AJ-16	AJ-17	Av.	AJ-18	AJ-19	AJ-20	AJ-21	Av.	MME-3	MME-5	MME-8	Av.
Quartz	32.74	35.06	30.36	32.52	32.67	32.86	31.03	29.85	36.22	32.49	7.12	7.49	9.21	7.94
Orthoclase	29.48	28.85	30.2	29.03	29.39	32.06	31.77	29.69	31.38	31.23	11.11	12.18	12.38	11.89
Albite	26	22.81	26.93	27.69	25.86	23.51	27.84	31.69	19.9	25.74	32.76	33.39	32.76	32.97
Anorthite	-	-	-	-	-	-	-	-	-	-	19.84	18.42	18.62	18.96
Acmite	2.27	2.29	2.36	2.14	2.27	2.1	1.93	1.79	2.07	1.97	-	-	-	-
Na-Metasilicate	1.42	2.81	1.71	1.21	1.79	1.8	0.25	0.29	2.91	1.31	-	-	-	-
Diopside	1.59	2.06	1.88	1.5	1.76	1.97	1.97	1.83	2.3	2.02	8.91	8.72	5.83	7.82
Hypersthene	5.93	5.57	5.98	5.32	5.70	5.19	4.78	4.52	4.65	4.79	15.6	15.26	16.73	15.86
Magnetite	-	-	-	-	-	-	-	-	-	-	1.83	1.78	1.72	1.78
Ilmenite	0.5	0.52	0.53	0.56	0.53	0.46	0.4	0.29	0.54	0.42	2.03	1.99	1.93	1.98
Apatite	0.04	0.02	0.02	0.02	0.03	0.04	0.02	0.04	0.02	0.03	0.7	0.67	0.72	0.70
Colour Index	8.02	8.15	8.39	7.37	7.98	7.62	7.15	6.63	7.49	7.22	28.37	27.75	26.21	27.44
Diff. Index	88	87	87	89	87.92	88	91	91	87	89.45	50.98	53.06	54.35	52.80

Table 3 : Rare earth element contents of Aja ring complex granites.

Rock type	Monzogranite				Syenogranite				Granophyre				Alkali feldspar granite				
Sample No.	AJ-1	AJ-2	AJ-3	Av.	AJ-4	AJ-5	AJ-6	Av.	AJ-7	AJ-8	AJ-9	Av.	AJ-11	AJ-12	AJ-13	AJ-14	Av.
La	31.15	36.82	50.57	39.51	62.28	63.48	74.63	66.80	82.11	95.65	124.12	100.63	136.12	146.08	130.9	110.81	130.98
Ce	69.49	82.14	106.68	86.10	133.67	135.04	163.39	144.03	190.46	203.69	243.86	212.67	279.81	270.89	287.09	263.66	275.36
Pr	9.39	11.1	14.29	11.59	17.33	18.66	20.62	18.87	23.32	23.87	32.41	26.53	34.84	37.15	35.05	36.76	35.95
Nd	37.65	44.49	56.23	46.12	68.59	74.89	85.69	76.39	99.31	91.94	124.98	105.41	132	145.3	138.25	152.34	141.97
Sm	7.72	9.13	10.9	9.25	13.84	14.52	17.01	15.12	25.41	19.73	22.2	22.45	24.46	29.26	28.15	30.36	28.06
Eu	0.51	0.59	0.74	0.61	0.99	0.59	1.23	0.94	1.46	1.34	1.23	1.34	1.29	1.72	1.83	1.59	1.61
Gd	7.19	8.39	9.8	8.46	12.76	10.74	13.68	12.39	26.72	16.72	18.94	20.79	21.85	23.57	22.42	23.43	22.82
Tb	1.07	1.26	1.47	1.27	1.95	1.76	2.13	1.95	4.09	2.78	2.66	3.18	3.22	3.44	3.28	3.23	3.29
Dy	6.17	7.29	8.53	7.33	11.74	10.66	13.13	11.84	24.57	18.06	14.98	19.20	19	17.73	20.53	19.78	19.26
Ho	1.21	1.43	1.67	1.44	2.3	2.08	2.56	2.31	4.99	3.93	2.78	3.90	3.66	3.66	4.11	3.85	3.82
Er	3.58	4.25	4.9	4.24	6.64	6.13	7.24	6.67	14.26	11.32	7.83	11.14	10.57	10.43	11.46	9.95	10.60
Tm	0.56	0.66	0.75	0.66	0.98	0.92	1.08	0.99	2.26	1.51	1.11	1.63	1.58	1.64	1.49	1.35	1.52
Yb	3.87	4.83	5.17	4.62	6.97	6.64	7.26	6.96	15.87	10.09	6.97	10.98	10.8	11.43	10.36	9.45	10.51
Lu	0.63	0.82	0.84	0.76	1.08	1.11	1.21	1.13	2.4	1.48	1.03	1.64	1.55	1.66	1.54	1.43	1.55
Eu/EU*	0.21	0.21	0.22	0.21	0.23	0.14	0.25	0.21	0.17	0.23	0.18	0.19	0.17	0.20	0.22	0.18	0.19
(La/Yb)n	5.44	5.16	6.61	5.74	6.04	6.46	6.95	6.49	3.50	6.41	12.04	7.32	8.52	8.64	8.54	7.93	8.41
((La/Sm)n	2.55	2.55	2.93	2.67	2.84	2.76	2.77	2.79	2.04	3.06	3.53	2.88	3.51	3.15	2.93	2.30	2.98
(Gd/Lu)n	1.40	1.25	1.43	1.36	1.45	1.19	1.39	1.34	1.36	1.38	2.25	1.67	1.73	1.74	1.78	2.01	1.81
(La/Lu)n	5.07	4.60	6.17	5.28	5.91	5.86	6.32	6.03	3.51	6.62	12.35	7.49	9.00	9.02	8.71	7.94	8.67

Table 3. Cont.

Rock type	Alkaline granite					Peralkaline granite					Mafic enclaves			
Sample No.	AJ-10	AJ-15	AJ-16	AJ-17	Av.	AJ-18	AJ-19	AJ-20	AJ-21	Av.	MME-3	MME-5	MME-8	Av.
La	127.91	146.95	156.83	180.18	152.97	212.42	242.48	300.5	263.06	254.62	17.38	16.68	16.09	16.72
Ce	262.49	324.25	341.43	351.13	319.83	452.46	519.18	657.35	569.01	549.50	37.7	35.77	34.51	35.99
Pr	32.26	38.85	42.8	45.59	39.88	56.02	59.96	76.89	65.69	64.64	4.76	4.54	4.43	4.58
Nd	132.58	160.18	166.22	182.36	160.34	215.27	241.75	304.92	258.88	255.21	20.43	19.39	18.53	19.45
Sm	27.82	33.47	33.11	35.49	32.47	41.76	48.13	64.61	49.63	51.03	4.18	3.96	3.44	3.86
Eu	0.93	1.72	1.64	1.76	1.51	1.92	2.21	2.33	2.48	2.24	1.4	1.27	1.02	1.23
Gd	22.86	28.65	29.98	28.8	27.57	37.61	37.94	51.14	42.03	42.18	3.25	3.15	2.69	3.03
Tb	3.45	4.2	4.53	4.15	4.08	5.26	5.79	7.61	5.91	6.14	0.39	0.37	0.33	0.36
Dy	22.61	27.41	25.78	27.71	25.88	32.75	36.76	46.72	36.51	38.19	2.47	2.19	1.95	2.20
Ho	4.68	5.46	4.93	5.52	5.15	6.43	7.08	9.18	7.25	7.49	0.4	0.36	0.32	0.36
Er	13.75	15.83	13.78	16.22	14.90	17.46	20.24	24.78	19.93	20.60	1	0.98	0.86	0.95
Tm	2.09	2.41	2.21	2.42	2.28	2.66	3.06	3.63	2.95	3.08	0.13	0.13	0.11	0.12
Yb	14.15	16.04	13.83	15.7	14.93	17.29	20.87	24.98	21.01	21.04	0.91	0.86	0.75	0.84
Lu	2.09	2.38	2.26	2.42	2.29	2.72	3.32	3.92	3.2	3.29	0.13	0.12	0.12	0.12
Eu/EU*	0.11	0.17	0.16	0.17	0.15	0.15	0.16	0.12	0.17	0.15	1.16	1.10	1.02	1.09
(La/Yb)n	6.11	6.20	7.67	7.76	6.93	8.31	7.86	8.13	8.47	8.19	12.92	13.12	14.51	13.51
((La/Sm)n	2.90	2.77	2.99	3.20	2.97	3.21	3.18	2.94	3.35	3.17	2.62	2.66	2.95	2.74
(Gd/Lu)n	1.34	1.48	1.63	1.46	1.47	1.69	1.40	1.60	1.61	1.58	3.06	3.22	2.75	3.01
(La/Lu)n	6.27	6.33	7.11	7.63	6.83	8.00	7.48	7.85	8.42	7.94	13.70	14.24	13.74	13.89